Journal of Computational Physics **167,** 247–276 (2001)
doi:10.1006/jcph.2000.6671, available online at http://www.idealibrary.com on IDEAL®

An Implicit Multigrid Method for Turbulent Combustion

Peter Gerlinger,* Helge Möbus,† and Dieter Brüggemann‡

*DLR-VT, Stuttgart, Pfaffenwaldring 38-40, 70569 Stuttgart, Germany; †Institut für Thermodynamik der Luft- und Raumfahrt, Universität Stuttgart, Pfaffenwaldring 31, 70550 Stuttgart, Germany, and ‡Lehrstuhl für Technische Thermodynamik, Universität Bayreuth, Universitätsstr. 30, 95440 Bayreuth, Germany
E-mail: peter.gerlinger@dlr.de

Received February 14, 2000; revised November 2, 2000

An implicit multigrid scheme for solving the Navier–Stokes, turbulence, species, and variance transport equations describing turbulent combustion is presented. Turbulence chemistry interaction is included by use of presumed probability density functions (pdf). To avoid stiffness problems associated with chemically reacting flows, time integration is performed by an implicit LU-SGS algorithm. This requires the formation of a source term Jacobian. The complete, analytically derived Jacobian, including assumed pdf modeling, is given in the present paper. Thus, the high numerical stability of the original algorithm is maintained. Convergence acceleration is accomplished by a nonlinear multigrid method. Strongly nonlinear source terms in species, turbulence, and variance conservation equations usually keep multigrid methods from converging. It is shown that freezing of coarse grid source terms including spatial derivatives and restriction damping in regions of high chemical activity may remedy this problem. Two finite-rate chemistry test cases with methane and hydrogen combustion at supersonic speed demonstrate a strong reduction in required CPU time.

Key Words: multigrid; combustion; supersonic flows; probability density function.

1. INTRODUCTION

The simulation of turbulent combustion is still a major challenge in the design of gas turbines and aircraft engines. In many cases fluctuations of temperature and species concentrations exert a significant influence on chemical production rates. An accurate prediction of high-speed combustors additionally requires complex chemistry. To account for turbulence–chemistry interaction, probability density functions (pdf) are used increasingly [1–5]. Two types of pdf approach can be distinguished: the evolution pdf method of Pope [1], which employs a Monte Carlo solver, and the assumed pdf method [3, 6, 7]. While for the first one the form of the pdf may evolve freely, it is presumed in the latter approach and completely

0021-9991/01 $35.00

defined knowing only the first couple of statistical moments. From a physical point of view the Monte Carlo pdf method is more accurate, but it requires substantially more computer resources. Additionally, methods for convergence acceleration that are widely used for moment methods are not available for Monte Carlo solvers. Thus, assumed pdf methods are computationally more attractive for complex three-dimensional simulations [4] or combustion processes that require a large number of different species. Implementation of variance equations into existing codes is straightforward and solution algorithms do not have to be changed.

Whether combustion is laminar or turbulent, finite-rate chemistry usually causes the system of governing equations to become numerically stiff. This is due to the widely disparate time and length scales resulting from chemical kinetics. Therefore, implicit or at least point-implicit methods are indispensable for numerical time integration. If the chemical source terms are linearized in time, source term Jacobians need to be formed. This should be done for arbitrary reaction schemes including three-body reactions with varying third-body efficiencies. Simplifications to the full source Jacobian resulting in a diagonal matrix are presented, for example, by Eberhardt and Imley [8]. However, the reduction in computer time consumption is usually paid for with smaller allowable time steps and a decrease in the robustness of the algorithm. Additionally, the time integration of species and total density become decoupled, which may cause problems in transient phases of time integration. Therefore, a fully implicit treatment of pdf and species source terms is introduced in this paper. It will be shown that the convergence properties of the original Lower–Upper Symmetric Gauss–Seidel (LU-SGS) algorithm are maintained after turbulence–chemistry interaction is included.

An implicit treatment of chemical source terms also has a stabilizing effect if multigrid is used for convergence acceleration [9]. It is possible to benefit from larger time steps at coarser grid levels if stability is not limited by stiffness resulting from chemical kinetics. Because the simulation of reactive flows still requires tremendous CPU time, convergence acceleration is of great importance. One of the most promising approaches for large problems is the multigrid method [10]. Excellent results have already been achieved for subsonic and transonic flows [11]. The combination of a full approximation storage (FAS) scheme for the nonlinear equations and a linearized defect correction already enables $O(Nm^2)$ solutions for transonic laminar test cases [12, 13], where N is the number of grid points and m the number of equations. Another promising approach uses different coarsening techniques according to the damping properties of different solvers [14]. While much progress has been achieved in this field for nonreactive flows, little work has been done on the use of multigrid solvers for combustion. The greatest problem in this context is the strong nonlinearity of chemical source terms that normally causes divergence of multigrid schemes. Because of this difficulty, Sheffer *et al.* [15] used only two grid levels for the simulation of detonation waves. Global damping of the restricted residual error is employed by Edwards [16] and local damping by Gerlinger *et al.* [9] to allow convergence with up to four grid levels. However, none of these publications included turbulence–chemistry interaction. The conservation equations for the variance of temperature and species fluctuations contain strongly nonlinear source terms too, causing additional problems. In the present paper the local damping of Ref. [9] and some additional modifications are introduced to enable convergence in conjunction with pdf modeling.

To our knowledge, this is the first paper in which detailed chemistry and an assumed pdf model are treated in a fully implicit fashion and the multigrid technique is used for convergence acceleration.

2. GOVERNING EQUATIONS AND NUMERICAL METHOD

The two-dimensional equations for chemically reacting flow can be written in a Cartesian coordinate system as

$$\frac{\partial \mathbf{Q}}{\partial t} + \frac{\partial (\mathbf{F} - \mathbf{F}_v)}{\partial x} + \frac{\partial (\mathbf{G} - \mathbf{G}_v)}{\partial y} = \mathbf{S}, \tag{1}$$

where the vector of conservative variables is

$$\mathbf{Q} = [\bar{\rho},\ \bar{\rho}\tilde{u},\ \bar{\rho}\tilde{v},\ \bar{\rho}\tilde{E},\ \bar{\rho}q,\ \bar{\rho}\omega,\ \bar{\rho}\sigma_e,\ \bar{\rho}\sigma_Y,\ \bar{\rho}\tilde{Y}_i]^T, \quad i = 1, 2, \ldots, N_k - 1, \tag{2}$$

F and **G** are inviscid, and, $\mathbf{F}_v$ and $\mathbf{G}_v$ are viscous fluxes in the x- and y-direction, respectively. The source vector **S** results from turbulence and chemistry. The Reynolds ($\bar{\ }$) or Favre ($\tilde{\ }$) averaged variables in Eq. (2) are density $\bar{\rho}$, velocity components $\tilde{u}$ and $\tilde{v}$, total specific energy $\tilde{E}$, turbulence variables $q = \sqrt{k}$ (k = turbulent kinetic energy) and $\omega = \epsilon/k$(ϵ = dissipation rate of k), variance of energy σ_e, species mass fractions $\tilde{Y}_i$, and the sum of their variances σ_Y. N_k denotes the number of different species. The simulation of hydrogen combustion involves a 9-species (N_2, O_2, H_2, H_2O, OH, O, H, HO_2, and H_2O_2), 19-step modified reaction scheme originally developed by Jachimowski [17] excluding the nitrogen reactions (see Table I). Slight modifications from the original scheme are taken from Ref. [18]. For methane combustion the simulation employs a 17-species (N_2, O_2, H_2,

TABLE I

Hydrogen–Air Combustion Mechanism[a]

j	Reaction[b] j	A_j	n_j	E_j
(1)	$H_2 + O_2 \rightleftharpoons HO_2 + H$	1.0×10^{14}	0	56,000
(2)	$H + O_2 \rightleftharpoons OH + O$	2.6×10^{14}	0	16,800
(3)	$O + H_2 \rightleftharpoons OH + H$	1.8×10^{10}	1.0	8,900
(4)	$OH + H_2 \rightleftharpoons H_2O + H$	2.2×10^{13}	0	5,150
(5)	$OH + OH \rightleftharpoons H_2O + O$	6.3×10^{12}	0	1,090
(6)	$H + OH + M \rightleftharpoons H_2O + M$	2.2×10^{22}	−2.0	0
(7)	$H + H + M \rightleftharpoons H_2 + M$	6.4×10^{17}	−1.0	0
(8)	$H + O + M \rightleftharpoons OH + M$	6.0×10^{16}	−0.6	0
(9)	$H + O_2 + M \rightleftharpoons HO_2 + M$	2.1×10^{15}	0	−1,000
(10)	$HO_2 + H \rightleftharpoons OH + OH$	1.4×10^{14}	0	1,080
(11)	$HO_2 + H \rightleftharpoons H_2O + O$	1.0×10^{13}	0	1,080
(12)	$HO_2 + O \rightleftharpoons O_2 + OH$	1.5×10^{13}	0	950
(13)	$HO_2 + OH \rightleftharpoons H_2O + O_2$	8.0×10^{12}	0	0
(14)	$HO_2 + HO_2 \rightleftharpoons H_2O_2 + O_2$	2.0×10^{12}	0	0
(15)	$H + H_2O_2 \rightleftharpoons H_2 + HO_2$	1.4×10^{12}	0	3,600
(16)	$O + H_2O_2 \rightleftharpoons OH + HO_2$	1.4×10^{13}	0	6,400
(17)	$OH + H_2O_2 \rightleftharpoons H_2O + HO_2$	6.1×10^{12}	0	1,430
(18)	$H_2O_2 + M \rightleftharpoons OH + OH + M$	1.2×10^{17}	0	45,500
(19)	$O + O + M \rightleftharpoons O_2 + M$	6.0×10^{13}	0	−1,800

[a] $k = AT^n \exp(-E/RT)$; units are seconds, moles, cubic centimeters, calories, and Kelvin.

[b] Third-body efficiencies relative to $N_2 = 1$ are as follows: For reaction (6), $H_2O = 6$; for reaction (7), $H_2 = 2$ and $H_2O = 6$; for reaction (8), $H_2O = 5$; for reaction (9), $H_2 = 2$ and $H_2O = 16$; and for reaction (18), $H_2O = 15$.

H_2O, OH, O, H, CH_3, CH_4, CH_2O, HCO, CO, H_2O_2, CH_2, HO_2, CH, and CO_2), 58-step reaction mechanism [19]. The reaction rate for methane dissociation (reaction (1) in Ref. [19]) is defined in a low- and high-pressure limit and is consequently difficult to treat implicitly. Therefore, this reaction is replaced by the corresponding reaction taken from Ref. [20]. A two-equation low-Reynolds-number q–ω model [9, 21] was chosen as turbulence closure.

The source vector appearing on the right-hand side of Eq. (1) is given by

$$\mathbf{S} = [0,\ 0,\ 0,\ 0,\ S_q,\ S_\omega,\ S_{\sigma_e},\ S_{\sigma_Y},\ S_i]^T, \quad i = 1, 2, \ldots, N_k - 1, \tag{3}$$

with source terms S_q and S_ω stemming from the q–ω turbulence model [21]; S_{σ_e} and S_{σ_Y} are source terms of the variance conservation equations, and S_i represents species source terms resulting from chemistry.

The unsteady form of governing equations is integrated in time using an implicit finite-volume LU-SGS algorithm [11, 22]. In addition to inviscid Jacobians, the implicit part includes simplified viscous Jacobians based on the thin-layer Navier–Stokes equations. An important measure to obtain numerical stability and to allow large time steps in the case of finite-rate chemistry is the implicit treatment of source vector $\mathbf{S}$ requiring the formation of a source Jacobian $\mathbf{H} = \partial\mathbf{S}/\partial\mathbf{Q}$. This Jacobian comprises contributions from turbulence, pdf modeling, and chemistry. Inviscid and viscous Jacobians for the pdf transport equations are formed in the same way as for the fluid variables [22]. Further details concerning the numerical scheme may be found in Ref. [9].

3. ASSUMED PDF CLOSURE

An assumed pdf method chosen to account for turbulence chemistry interaction is applied to determine averaged species and pdf production rates. The instantaneous production rate of species i is given by

$$S_i = M_i \sum_{r=1}^{N_r} \left[(\nu''_{ir} - \nu'_{ir}) \left(k_{f_r} \prod_{l=1}^{N_k+1} c_l^{\nu'_{lr}} - k_{b_r} \prod_{l=1}^{N_k+1} c_l^{\nu''_{lr}} \right) \right], \tag{4}$$

where N_r denotes the number of reactions involved. Because transport equations are solved for $N_k - 1$ species only, the concentration of the last species must be expressed through the normalization property

$$c_{N_k} = \frac{\rho Y_{N_k}}{M_{N_k}} = \frac{1}{M_{N_k}} \left(\rho - \sum_{i=1}^{N_k-1} \rho Y_i \right), \tag{5}$$

which becomes important for the source Jacobian formation. M_i denotes the molecular weight of species i and concentration

$$c_{N_k+1} = \sum_{i=1}^{N_k-1} \left(\frac{t_i}{M_i} - \frac{t_{N_k}}{M_{N_k}} \right) \rho Y_i + \rho \frac{t_{N_k}}{M_{N_k}} \tag{6}$$

represents third-body species with t_i being the respective third-body efficiency. The stoichiometric coefficient of reactant $N_k + 1$ is 1 if three-body reactions take place; otherwise

it is 0. If the one-point one-time joint pdf of temperature and composition, P, is known, the mean production rate can be determined from

$$\overline{S_i} = \int S_i\left(\hat{T}, \hat{c}_1, \ldots, \hat{c}_{N_k}\right) P\left(\hat{T}, \hat{c}_1, \ldots, \hat{c}_{N_k}\right) d\hat{T}\, d\hat{c}_1 \ldots d\hat{c}_{N_k} \tag{7}$$

by integrating over all realizable states of sample space variables $\hat{T}$ and $\hat{c}_i$. Using a presumed pdf concept, the shape of the pdf P has a mathematical form that is defined in the present case by the variable's mean and one higher order correlation. We follow the approaches of Girimaji [7, 23], Gaffney *et al*. [24], and Baurle [3, 4] and assume a Gaussian distribution for temperature and a multivariate β-pdf model for species mass fractions. One of the shortcomings of this approach is that statistical independence of temperature, composition, and density must be assumed. Thus, the pdf P can be written as the product of marginal pdfs

$$P\left(\hat{T}, \hat{c}_1, \ldots, \hat{c}_{N_k}\right) = P_T(\hat{T}) P_Y\left(\hat{Y}_1, \ldots, \hat{Y}_{N_k}\right) \delta(\hat{\rho} - \overline{\rho}). \tag{8}$$

This considerably simplifies the integration of Eq. (7), which now may be performed in consecutive steps

$$\overline{S_i} = M_i \sum_{r=1}^{N_r} \left[(\nu''_{ir} - \nu'_{ir}) \cdot \left(\overline{k_{f_r}} \overline{\prod_{l=1}^{N_k+1} \left(\frac{\overline{\rho} Y_l}{M_l} \right)^{\nu'_{lr}}} - \overline{k_{b_r}} \overline{\prod_{l=1}^{N_k+1} \left(\frac{\overline{\rho} Y_l}{M_l} \right)^{\nu''_{lr}}} \right) \right]. \tag{9}$$

Baurle and Girimaji [25] propose a new approach for assumed pdfs that also accounts for temperature–composition correlations, which are neglected in the present paper.

3.1. *Assumed PDF of Temperature*

The pdf of temperature, $P_T(\hat{T})$, is assumed to be Gaussian distribution [4]

$$P_T(\hat{T}) = \frac{1}{\sqrt{2\pi\sigma_T}} \exp\left[-\frac{(\hat{T} - \tilde{T})^2}{2\sigma_T} \right], \quad \sigma_T = \widetilde{T''^2}, \tag{10}$$

fully determined by its first and second moments. While the first moment, $\tilde{T}$, results from the averaged energy equation, an additional conservation equation becomes necessary for the second central moment, the energy variance, σ_e, which is related to the temperature variance σ_T. Due to presumed statistical independence, time-averaged forward and backward reaction rates of reaction r are obtained from

$$\overline{k_r} = \int_{\hat{T}=0}^{\hat{T}=\infty} k_r(\hat{T}) P_T(\hat{T})\, d\hat{T}. \tag{11}$$

Since no analytical solution for this integral exists, it has to be calculated numerically. In practice, integration cannot be performed over an infinite temperature range. Following Baurle [26], lower and upper temperature integration limits are introduced that cover the relevant part of the temperature range. A second restriction is the limited validity of the Arrhenius function (e.g., temperatures above 3000 K often lead to significant errors). Therefore, the pdf is clipped at lower and upper limits and significant parts of the pdf may

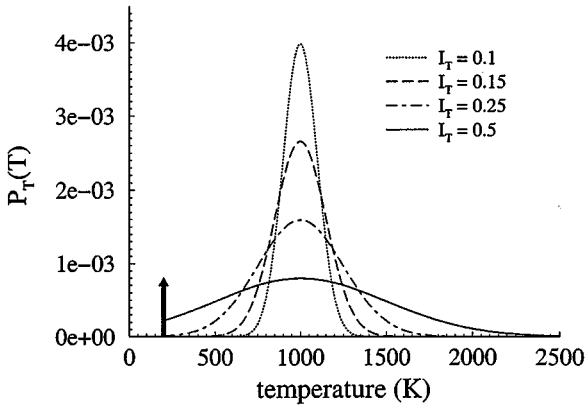

FIG. 1. Gaussian pdfs for $\tilde{T} = 1000$ K and different temperature fluctuation intensities I_T.

be lost. In order not to violate the normalization property of the pdf, Dirac delta functions are added at the clipped ends (at $T_{\min}$ and $T_{\max}$), and Eq. (10) is replaced by

$$P_T(\hat{T}) = \frac{1}{\sqrt{2\pi\sigma_0}} \exp\left[-\frac{(\hat{T}-\tilde{T}_0)^2}{2\sigma_0}\right][H(\hat{T}-T_{\min}) - H(\hat{T}-T_{\max})] + A_1\delta(\hat{T}-T_{\min}) + A_2\delta(\hat{T}-T_{\max}), \tag{12}$$

using the Heaviside function H, where A_1 and A_2 correspond to the areas of the clipped tails [6]. The free parameters $\tilde{T}_0$ and σ_0 are determined by a Newton–Raphson iteration in such a way that the first and second moments remain unaltered in comparison with the unclipped distribution. Figure 1 shows Gaussian distributions for $\tilde{T} = 1000$ K with temperature fluctuation intensities $I_T = \sqrt{\sigma_T}/\tilde{T}$ of 0.1, 0.15, 0.25, and 0.5. For $I_T = 0.5$ the pdf is clipped at 200 K, and a delta function is added.

The numerical integration of Eq. (11) is performed by Simson's rule. To avoid this integration at every time step, look-up tables are used for averaged forward and backward reaction rates. Intermediate values can be interpolated from tabulated values depending on mean temperature $\tilde{T}$ and temperature fluctuation intensity I_T. This follows the approach of Baurle [3, 26], who used look-up tables for $\bar{k}_f$ and $\bar{k}_b$. However, there may be very large gradients in the distribution of reaction rates. Therefore, we did not store the averaged reaction rates directly, but the ratio of averaged to laminar reaction rates, $\alpha_f = \bar{k}_f/k_f$ and $\alpha_b = \bar{k}_b/k_b$, to eliminate the exponential dependence on temperature. This treatment results in a smoother distribution and, consequently, improved accuracy of the interpolation algorithm. On the other hand, this normalization necessitates the recalculation of laminar reaction rates at every time step. Table II shows a comparison of both treatments for selected reactions of the Jachimowski hydrogen–air reaction mechanism of Table I. The center values between four surrounding tabulated points are calculated with both interpolation methods and are compared with exact values. Because low temperatures cause extreme, but insignificant values of α, errors are evaluated only for $\tilde{T} > 500$ K and $\alpha < 10^7$. Table II displays results for selected forward (f) and backward (b) reactions, including those of largest errors. $\epsilon_{\max}$ is the maximum relative error of all values within the table and ϵ_{av} the average relative error (over all values), each in comparison with the exact value. The last column shows the relative reduction in average error resulting from the use of normalized

TABLE II
Interpolation Errors (%) by Use of Two Different Look-Up Tables Compared with Exact Values[a]

j	$\epsilon_{\max,1}$	$\epsilon_{\text{av},1}$	$\epsilon_{\max,2}$	$\epsilon_{\text{av},2}$	Improvement
2f	2.17	0.055	4.77	0.15	63.
2b	0.01	0.0003	0.01	0.001	74.
4f	0.15	0.004	0.31	0.010	56.
4b	3.39	0.089	7.33	0.224	60.
9f	0.23	0.004	0.23	0.009	53.
9b	11.5	0.368	12.4	0.620	41.
19f	11.4	0.395	17.5	0.751	47.
19b	3.10	0.300	3.10	0.342	12.

[a] Index 1 indicates tabulation of $\bar{k}/k$; index 2 indicates tabulation of $\bar{k}$.

reaction rates instead of absolute ones. While for the maximum error there are a few reactions for which the normalization aggravated the results slightly, the average errors are always reduced significantly. In the present case the table consists of 170 points in mean temperature direction and 85 points in I_T direction.

Besides the mean temperature, the variance is needed as a second parameter to fully define the shape of the Gaussian pdf. An equation for the variance of enthalpy or energy can easily be derived from the energy or enthalpy equation. Another possibility is to use equations for the variance in sensible energy or sensible enthalpy. If sensible quantities are opted for, the temperature variance may be determined more accurately because this approach involves less assumptions (concerning particularily enthapies of formation). On the other hand, variance equations for sensible quantities contain an additional source term (here for the energy variance equation)

$$-\overline{2e_s'' \sum_{k=1}^{N_k} S_k h_{f,k}} \tag{13}$$

that involves the pdf to calculate a higher order turbulent moment (h_f denotes the enthalpy of formation). Because the shape of the pdf has a much larger influence on this term than on turbulent reaction rates, large discrepancies may be expected in regions with incorrect shape. Additionally, this term is difficult to include in the source Jacobian for time integration and has to be stored in look-up tables, too. Therefore, we opted for a conservation equation for the variance of energy. Energy is chosen because there are less modeling assumptions involved than with enthalpy [24]. The modeled conservation equation for variance of energy is given by

$$\begin{aligned} &\frac{\partial}{\partial t}(\bar{\rho}\sigma_e) + \frac{\partial}{\partial x_j}(\bar{\rho}\tilde{u}_j\sigma_e) - \frac{\partial}{\partial x_j}\left[\left(\frac{\mu}{\text{Pr}} + \frac{\mu_t}{\text{Pr}_t}\right)\frac{\partial \sigma_e}{\partial x_j}\right] \\ &\quad = \underbrace{2\frac{\mu_t}{\text{Pr}_t}\left(\frac{\partial \tilde{e}}{\partial x_j}\right)^2}_{S_{e1}} - C_e\bar{\rho}\sigma_e\omega - 2(\hat{\gamma}-1)\bar{\rho}\sigma_e\underbrace{\frac{\partial \tilde{u}_j}{\partial x_j}}_{S_{e2}}, \end{aligned} \tag{14}$$

with $\sigma_e = \widetilde{e''^2}$. Unclosed correlations are modeled with gradient-type approximations [24, 26], the laminar and turbulent Prandtl numbers, Pr and Pr_t, are 0.7 and 0.9, respectively, the

model constant C_e equals 0.5, $\hat{\gamma}$ denotes the ratio of specific heats, and $\omega = 1/\tau$, where τ is a turbulent time scale. All terms on the right-hand side of Eq. (14) represent source terms, and the first one, S_{e1}, represents main production. The spatial derivatives within these terms cause problems if multigrid methods are applied and therefore require a special treatment described later. Using an averaged specific heat

$$\hat{c}_v = \hat{c}_v(\tilde{T}, \tilde{Y}_k) = \sum_{k=1}^{N_k} \tilde{Y}_k \frac{\int_0^{\tilde{T}} c_{v_k}(\tilde{T})\, d\tilde{T}}{\tilde{T}}, \tag{15}$$

we can recover the temperature variance from energy variance by

$$\widetilde{T''^2} \approx \frac{\widetilde{e''^2}}{\hat{c}_v^2}, \tag{16}$$

neglecting effects of species fluctuations on $\hat{c}_v$ and on the heat of formation.

3.2. *Assumed PDF of Composition*

Following Girimaji [7, 23], a multivariate β distribution describes the pdf of composition. A great advantage of this pdf is that, besides the first moments of species mass fractions, just one additional second moment, the sum of species mass fraction variances,

$$\sigma_Y = \sum_{m=1}^{N_k} \widetilde{Y_m''^2}, \tag{17}$$

suffices to parametrize its shape. Another presumption to allow the calculation of multicomponent flows is the existence of an analytical solution of the integral involving the pdf, which is also met. The pdf of composition is given by [7]

$$P\left(\hat{Y}_1, \hat{Y}_2, \ldots, \hat{Y}_{N_k}\right) = \frac{\Gamma\left(\sum_{m=1}^{N_k} \beta_m\right)}{\prod_{m=1}^{N_k} \Gamma(\beta_m)} \cdot \delta\left(1 - \sum_{m=1}^{N_k} \hat{Y}_m\right) \cdot \prod_{m=1}^{N_k} \hat{Y}_m^{\beta_m - 1}, \tag{18}$$

with parameters

$$\beta_m = \tilde{Y}_m B, \quad B = \frac{\sum_{m=1}^{N_k} \tilde{Y}_m (1 - \tilde{Y}_m)}{\sigma_Y} - 1. \tag{19}$$

Equation (18) is only valid if $0 \leq \beta_m \leq \infty$. This realizability condition is satisfied if

$$\sigma_Y \leq \sum_{m=1}^{N_k} \tilde{Y}_m (1 - \tilde{Y}_m). \tag{20}$$

Because a separate conservation equation is employed to calculate σ_Y, this constraint is not satisfied automatically by the numerical solution. However, problems only arise if the mass fraction of one species approaches 1. In this case both sides of Eq. (20) approach zero, while their ratio, appearing in Eq. (19), must tend to infinity. Under these circumstances even extremely small fluctuations σ_Y can have a maximum influence on chemical production

rates. Because this problem only arises if one species is close (or identical) to one, it mainly affects decomposition reactions such as $CH_4 + M \rightarrow CH_3 + H + M$. Limiting B as well as σ_Y (by Eq. (20)) circumvents this problem.

It should also be noted that the calculation of averaged production rates requires Reynolds-averaged mass fractions to define the pdf. The use of Favre-averaged quantities instead thus is an additional simplification.

As may be seen from Eqs. (18) and (19), the multivariate β-pdf is completely defined by mean values $\tilde{Y}_m$ obtained from species conservation equations and σ_Y, for which an additional equation is needed. This equation can be derived from the species conservation equations [7, 26], and its modeled form is given by

$$\frac{\partial}{\partial t}(\bar{\rho}\sigma_Y) + \frac{\partial}{\partial x_j}(\bar{\rho}\tilde{u}_j\sigma_Y) - \frac{\partial}{\partial x_j}\left[\bar{\rho}(D + D_t)\frac{\partial \sigma_Y}{\partial x_j}\right] = \underbrace{2\sum_{i=1}^{N_k}\bar{\rho}D_t\frac{\partial \tilde{Y}_i}{\partial x_j}\frac{\partial \tilde{Y}_i}{\partial x_j}}_{S_{Y1}} - C_{\sigma_Y}\bar{\rho}\sigma_Y\omega + 2\sum_{i=1}^{N_k}\overline{Y_i'' S_i}. \tag{21}$$

Again, unclosed correlations are modeled with gradient-type approximations [4, 24], D and D_t denote laminar and turbulent diffusion coefficients, and the model constant C_{σ_Y} equals 0.5. All terms on the right-hand side represent source terms. The first one, S_{Y1}, constitutes main production; the second one is dissipation. The last term is calculated analytically with known pdf and needs no further modeling. This term causes a strong dissipation of σ_Y in the main reaction zone.

3.3. *Species Production Terms*

Because of the assumed statistical independence of temperature and species fluctuations, the averaged forward and backward reaction rates may be treated separately from the remaining parts [26]. The term that requires integration over the mass fraction pdf

$$\overline{\prod_{l=1}^{N_k+1}\left(\frac{Y_l}{M_l}\right)^{\nu_{lr}}} = \int\left(\sum_{j=1}^{N_k}\frac{t_j\hat{Y}_j}{M_j}\right)^{\nu_{N_k+1r}}\left(\prod_{l=1}^{N_k}\hat{Y}_l^{\nu_{lr}}\right)P(\hat{Y}_1, \hat{Y}_2, \ldots \hat{Y}_{N_k})\, d\hat{Y}_1\, d\hat{Y}_2 \ldots d\hat{Y}_{N_k}$$
$$= \frac{\prod_{j=1}^{N_k}\prod_{l=1}^{\nu_{jr}}(\beta_j + \nu_{jr} - l)}{\prod_{j=1}^{m_r}(B + m_r - j)}\underbrace{\left[\sum_{j=1}^{N_k}\frac{t_j}{M_j}(\beta_j + \nu_{jr})\right]^{\nu_{N_k+1r}}}_{\neq 1 \text{ only for 3-body reactions}} \tag{22}$$

is solved analytically with

$$m_{fr} = \sum_{j=1}^{N_k+1}\nu'_{jr}, \quad m_{br} = \sum_{j=1}^{N_k+1}\nu''_{jr}, \tag{23}$$

including three-body reactions. Thus the total averaged production rate of species i finally evolves from

$$\overline{S_i} = M_i\sum_{r=1}^{N_r}(\nu''_{ir} - \nu'_{ir})(T_{1f}T_{2f}T_{3f}T_{4f} - T_{1b}T_{2b}T_{3b}T_{4b}), \tag{24}$$

with contributions

$$T_1 = \bar{k}_r, \tag{25}$$

$$T_2 = \bar{\rho}^{\nu_{N_k+1r}} \prod_{l=1}^{N_k} \left(\frac{\bar{\rho}}{M_l}\right)^{\nu_{lr}} = \bar{\rho}^{m_r} \prod_{l=1}^{N_k} \left(\frac{1}{M_l}\right)^{\nu_{lr}}, \tag{26}$$

$$T_3 = \frac{\prod_{j=1}^{N_k} \prod_{l=1}^{\nu_{jr}} (\beta_j + \nu_{jr} - l)}{\prod_{j=1}^{m_r} (B + m_r - j)} =: \frac{P_1}{P_2}, \tag{27}$$

$$T_4 = \left[\sum_{j=1}^{N_k} \frac{t_j}{M_j} (\beta_j + \nu_{jr})\right]^{\nu_{N_k+1r}}. \tag{28}$$

These terms are functions of the variables $T_1 = T_1(\tilde{T}, I_T)$, $T_2 = T_2(\bar{\rho})$, $T_3 = T_3(\tilde{Y}_i, \sigma_Y)$, $T_4 = T_4(\tilde{Y}_i, \sigma_Y)$, and P_1, P_2 are defined for later use. Again, because of the exponent ν_{N_k+1r}, term, T_4 has only to be calculated in case of three-body reactions and otherwise becomes 1.

3.4. *Species Variance Production Terms*

An additional source term that requires integration over the composition pdf is the last one appearing in the species variance equation (21),

$$\sum_{i=1}^{N_k} \overline{Y_i'' S_i} = \sum_{i=1}^{N_k} (\overline{Y_i S_i} - \tilde{Y}_i \overline{S_i}). \tag{29}$$

While the second contribution to the sum on the right-hand side is known from above, the first part remains to be determined. The calculation of $\overline{Y_i S_i}$ requires the integration [26]

$$\begin{aligned} &\int \hat{Y}_i \left(\sum_{j=1}^{N_k} \frac{t_j \hat{Y}_j}{M_j}\right)^{\nu_{N_k+1r}} \left(\prod_{l=1}^{N_k} \hat{Y}_l^{\nu_{lr}}\right) P\left(\hat{Y}_1, \hat{Y}_2, \ldots \hat{Y}_{N_k}\right) d\hat{Y}_1 \, d\hat{Y}_2 \ldots d\hat{Y}_{N_k} \\ &= \frac{\beta_i + \nu_{ir}}{B + m_r} \frac{\prod_{j=1}^{N_k} \prod_{l=1}^{\nu_{jr}} (\beta_j + \nu_{jr} - l)}{\prod_{j=1}^{m_r} (B + m_r - j)} \underbrace{\left[\frac{t_i}{M_i} + \sum_{j=1}^{N_k} \frac{t_j}{M_j} (\beta_j + \nu_{jr})\right]^{\nu_{N_k+1r}}}_{\neq 1 \text{ only for 3-body reactions}}, \end{aligned} \tag{30}$$

and the source term contributing to Eq. (29) is obtained from

$$\overline{Y_i S_i} = M_i \sum_{r=1}^{N_r} (\nu_{ir}'' - \nu_{ir}')(T_{1f} T_{2f} T_{3f} T_{5f} T_{6f} - T_{1b} T_{2b} T_{3b} T_{5b} T_{6b}). \tag{31}$$

Both T_5 and T_6 are new functions depending on $\tilde{Y}_i$ and σ_Y,

$$T_5 = \frac{\beta_i + \nu_{ir}}{B + m_r} =: \frac{P_3}{P_4}, \tag{32}$$

$$T_6 = \left[\frac{t_i}{M_i} + \sum_{j=1}^{N_k} \frac{t_j}{M_j} (\beta_j + \nu_{jr})\right]^{\nu_{N_k+1r}}. \tag{33}$$

In accordance with term T_4 given in Eq. (28), T_6 has to be calculated for three-body reactions only and otherwise becomes 1.

4. SOURCE TERM JACOBIAN

As described before, source terms are treated in a completely implicit fashion as to mitigate stiffness problems resulting from finite-rate chemistry. In the context of LU-SGS algorithms, the implicit treatment of chemical source terms has proven to be very stable and to allow large CFL numbers for a great variety of different combustion problems [9, 22, 27–29]. Moreover, high numerical stability is a requirement for the use of multigrid methods in case of combustion. The complete source Jacobian due to laminar chemistry is given in Ref. [22]. The formation of the source Jacobian including assumed pdf modeling introduces additional complexity. For maximum stability, backward Euler discretization is employed with linearization about the initial state. If source terms resulting from axisymmetry are neglected, the source Jacobian has the general form

$$\mathbf{H} = \begin{bmatrix}
0 & 0 & 0 & 0 & 0 & 0 & 0 & 0 & 0 & \dots & 0 \\
\vdots & \vdots & \vdots & \vdots & \vdots & \vdots & \vdots & \vdots & \vdots & \vdots & \vdots \\
0 & 0 & 0 & 0 & 0 & 0 & 0 & 0 & 0 & \dots & 0 \\
\frac{\partial S_q}{\partial \bar{\rho}} & 0 & 0 & 0 & \frac{\partial S_q}{\partial(\bar{\rho}q)} & \frac{\partial S_q}{\partial(\bar{\rho}\omega)} & 0 & 0 & 0 & \dots & 0 \\
\frac{\partial S_\omega}{\partial \bar{\rho}} & 0 & 0 & 0 & \frac{\partial S_\omega}{\partial(\bar{\rho}q)} & \frac{\partial S_\omega}{\partial(\bar{\rho}\omega)} & 0 & 0 & 0 & \dots & 0 \\
\frac{\partial S_{\sigma_e}}{\partial \bar{\rho}} & 0 & 0 & 0 & 0 & \frac{\partial S_{\sigma_e}}{\partial(\bar{\rho}\omega)} & \frac{\partial S_{\sigma_e}}{\partial(\bar{\rho}\sigma_e)} & \frac{\partial S_{\sigma_e}}{\partial(\bar{\rho}\sigma_Y)} & 0 & \dots & 0 \\
\frac{\partial S_{\sigma_Y}}{\partial \bar{\rho}} & \frac{\partial S_{\sigma_Y}}{\partial(\bar{\rho}\tilde{u})} & \frac{\partial S_{\sigma_Y}}{\partial(\bar{\rho}\tilde{v})} & \frac{\partial S_{\sigma_Y}}{\partial(\bar{\rho}\tilde{E})} & \frac{\partial S_{\sigma_Y}}{\partial(\bar{\rho}q)} & \frac{\partial S_{\sigma_Y}}{\partial(\bar{\rho}\omega)} & \frac{\partial S_{\sigma_Y}}{\partial(\bar{\rho}\sigma_e)} & \frac{\partial S_{\sigma_Y}}{\partial(\bar{\rho}\sigma_Y)} & \frac{\partial S_{\sigma_Y}}{\partial(\bar{\rho}\tilde{Y}_1)} & \cdots & \frac{\partial S_{\sigma_Y}}{\partial(\bar{\rho}\tilde{Y}_n)} \\
\frac{\partial S_1}{\partial \bar{\rho}} & \frac{\partial S_1}{\partial(\bar{\rho}\tilde{u})} & \frac{\partial S_1}{\partial(\bar{\rho}\tilde{v})} & \frac{\partial S_1}{\partial(\bar{\rho}\tilde{E})} & \frac{\partial S_1}{\partial(\bar{\rho}q)} & \frac{\partial S_1}{\partial(\bar{\rho}\omega)} & \frac{\partial S_1}{\partial(\bar{\rho}\sigma_e)} & \frac{\partial S_1}{\partial(\bar{\rho}\sigma_Y)} & \frac{\partial S_1}{\partial(\bar{\rho}\tilde{Y}_1)} & \cdots & \frac{\partial S_1}{\partial(\bar{\rho}\tilde{Y}_n)} \\
\vdots & \vdots & \vdots & \vdots & \vdots & \vdots & \vdots & \vdots & \vdots & \vdots & \vdots \\
\frac{\partial S_n}{\partial \bar{\rho}} & \frac{\partial S_n}{\partial(\bar{\rho}\tilde{u})} & \frac{\partial S_n}{\partial(\bar{\rho}\tilde{v})} & \frac{\partial S_n}{\partial(\bar{\rho}\tilde{E})} & \frac{\partial S_n}{\partial(\bar{\rho}q)} & \frac{\partial S_n}{\partial(\bar{\rho}\omega)} & \frac{\partial S_n}{\partial(\bar{\rho}\sigma_e)} & \frac{\partial S_n}{\partial(\bar{\rho}\sigma_Y)} & \frac{\partial S_n}{\partial(\bar{\rho}\tilde{Y}_1)} & \cdots & \frac{\partial S_n}{\partial(\bar{\rho}\tilde{Y}_n)}
\end{bmatrix}, \tag{34}$$

where index n denotes species $N_k - 1$. The turbulence variables q and ω are treated as loosely coupled with fluid motion. Matrix $\mathbf{H}$ has to be inverted at every grid point and time step, but the lines of q, ω, and σ_e can be treated separately to reduce this effort. While the source term Jacobian has to be formed with respect to the conservative variable vector, $\mathbf{Q}$, the species source terms $\overline{S_i}$ are explicit functions of primitive variables; i.e.,

$$\overline{S_i} = f\left(\tilde{T}, I_T, \sigma_Y, \tilde{c}_1, \tilde{c}_2, \dots, \tilde{c}_{N_k}\right). \tag{35}$$

The elements of the Jacobian matrix may be calculated using the chain rule for partial derivatives. Beside the conservative variable vector given in Eq. (2), two additional variable vectors

$$\mathbf{Q^1} = [\bar{\rho},\ \bar{\rho}\tilde{u},\ \bar{\rho}\tilde{v},\ \tilde{T},\ \bar{\rho}q,\ \bar{\rho}\omega,\ I_T,\ \sigma_Y,\ \bar{\rho}\tilde{Y}_i]^T, \tag{36}$$

$$\mathbf{Q^2} = [\bar{\rho},\ \bar{\rho}\sigma_e,\ \tilde{T},\ \bar{\rho}\tilde{Y}_i]^T, \tag{37}$$

with $i = 1, 2, \dots, N_k - 1$ are needed in the chain rule procedure. To facilitate the evaluation of Jacobian matrix elements, we first define some derivatives with respect to the new variable vectors that are used later.

As mentioned before, look-up tables are employed for normalized turbulent forward and backward reaction rates, $\alpha = \bar{k}/k$, depending on $\tilde{T}$ and I_T. Because no analytical solution exists, derivatives of these terms with respect to temperature and temperature fluctuation intensity must be calculated numerically from tabulated values. Four surrounding points are used to obtain gradients $\partial\alpha/\partial\tilde{T}$ and $\partial\alpha/\partial I_T$. While the laminar reaction rate $k = k(\tilde{T})$ is a function of temperature only, its turbulent counterpart $\bar{k} = \alpha k = \bar{k}(\tilde{T}, I_T)$ additionally depends on temperature fluctuation intensity so that the corresponding derivatives are

$$\left.\frac{\partial\bar{k}}{\partial\tilde{T}}\right|_{\mathbf{Q^1}\setminus\tilde{T}} = k\left.\frac{\partial\alpha}{\partial\tilde{T}}\right|_{\mathbf{Q^1}\setminus\tilde{T}} + \alpha\left.\frac{\partial k}{\partial\tilde{T}}\right|_{\mathbf{Q^1}\setminus\tilde{T}}, \tag{38}$$

$$\left.\frac{\partial\bar{k}}{\partial I_T}\right|_{\mathbf{Q^1}\setminus I_T} = k\left.\frac{\partial\alpha}{\partial I_T}\right|_{\mathbf{Q^1}\setminus I_T}. \tag{39}$$

For all partial derivatives the \ indicates that the following dependent variable, e.g., $\tilde{T}$ in Eq. (38), is allowed to change while all remaining variables of the corresponding vector, e.g., $\mathbf{Q^1}$, stay constant. Arrhenius functions are used for forward ($k_f = A\tilde{T}^n \exp(E/R_m\tilde{T})$) and equilibrium constants K_ϑ for backward ($k_b = k_f/K_\vartheta$) reaction rates. When these are inserted into the above equation, the final expressions for reaction rate derivatives

$$\left.\frac{\partial\bar{k}_f}{\partial\tilde{T}}\right|_{\mathbf{Q^1}\setminus\tilde{T}} = k_f\left.\frac{\partial\alpha_f}{\partial\tilde{T}}\right|_{\mathbf{Q^1}\setminus\tilde{T}} + \frac{\bar{k}_f}{\tilde{T}}\left(n + \frac{E}{R_m\tilde{T}}\right), \tag{40}$$

$$\left.\frac{\partial\bar{k}_b}{\partial\tilde{T}}\right|_{\mathbf{Q^1}\setminus\tilde{T}} = k_b\left.\frac{\partial\alpha_b}{\partial\tilde{T}}\right|_{\mathbf{Q^1}\setminus\tilde{T}} + \frac{\bar{k}_b}{\tilde{T}}\left(n + \sum_{j=1}^{N_k}\nu_j + \frac{E}{R_m\tilde{T}} - \frac{\tilde{T}}{K_\vartheta}\frac{\partial K_\vartheta}{\partial\tilde{T}}\right) \tag{41}$$

are obtained. With these expressions the temperature and variance intensity derivatives of $\overline{S_i}$ follow as

$$\left.\frac{\partial\overline{S_i}}{\partial\tilde{T}}\right|_{\mathbf{Q^1}\setminus\tilde{T}} = M_i\sum_{r=1}^{N_r}(\nu''_{ir} - \nu'_{ir})\left[\left.\frac{\partial\bar{k}_{f_r}}{\partial\tilde{T}}\right|_{\mathbf{Q^1}\setminus\tilde{T}} T_{2f}T_{3f}T_{4f} - \left.\frac{\partial\bar{k}_{b_r}}{\partial\tilde{T}}\right|_{\mathbf{Q^1}\setminus\tilde{T}} T_{2b}T_{3b}T_{4b}\right], \tag{42}$$

$$\left.\frac{\partial\overline{S_i}}{\partial I_T}\right|_{\mathbf{Q^1}\setminus I_T} = M_i\sum_{r=1}^{N_r}(\nu''_{ir} - \nu'_{ir})\left[\left.\frac{\partial\bar{k}_{f_r}}{\partial I_T}\right|_{\mathbf{Q^1}\setminus I_T} T_{2f}T_{3f}T_{4f} - \left.\frac{\partial\bar{k}_{b_r}}{\partial I_T}\right|_{\mathbf{Q^1}\setminus I_T} T_{2b}T_{3b}T_{4b}\right]. \tag{43}$$

In the same way, derivatives of the composition variance source term, given in Eq. (31), are formed:

$$\left.\frac{\partial(\overline{Y_iS_i})}{\partial\tilde{T}}\right|_{\mathbf{Q^1}\setminus\tilde{T}} = M_i\sum_{r=1}^{N_r}(\nu''_{ir} - \nu'_{ir})\left[\left.\frac{\partial\bar{k}_{f_r}}{\partial\tilde{T}}\right|_{\mathbf{Q^1}\setminus\tilde{T}} T_{2f}T_{3f}T_{5f}T_{6f} - \left.\frac{\partial\bar{k}_{b_r}}{\partial\tilde{T}}\right|_{\mathbf{Q^1}\setminus\tilde{T}} T_{2b}T_{3b}T_{5b}T_{6b}\right], \tag{44}$$

$$\left.\frac{\partial(\overline{Y_iS_i})}{\partial I_T}\right|_{\mathbf{Q^1}\setminus I_T} = M_i\sum_{r=1}^{N_r}(\nu''_{ir} - \nu'_{ir})\left[\left.\frac{\partial\bar{k}_{f_r}}{\partial I_T}\right|_{\mathbf{Q^1}\setminus I_T} T_{2f}T_{3f}T_{5f}T_{6f} - \left.\frac{\partial\bar{k}_{b_r}}{\partial I_T}\right|_{\mathbf{Q^1}\setminus I_T} T_{2b}T_{3b}T_{5b}T_{6b}\right]. \tag{45}$$

Finally, the remaining derivatives needed for later use are

$$\left.\frac{\partial \tilde{T}}{\partial \tilde{e}}\right|_{\mathbf{Q}\setminus\overline{\rho}\tilde{E}} = \frac{1}{c_v}, \tag{46}$$

$$\left.\frac{\partial \tilde{e}}{\partial \overline{\rho}}\right|_{\mathbf{Q}\setminus\overline{\rho}} = \frac{1}{\overline{\rho}}(\tilde{u}^2 + \tilde{v}^2 + 2q^2 - \tilde{E}). \tag{47}$$

In the case of laminar chemistry ($\sigma_T = 0$ and $\alpha = 1$) all derivatives of α disappear and the derivatives of reaction rates given in Eqs. (40) and (41) approach their laminar values.

4.1. *Derivatives of Composition PDF Parameters*

Because the continuity equation is included in the set of governing equations, only $N_k - 1$ concentrations are independent for a system of N_k different species. Therefore, the composition pdf parameters β_j first have to be expressed as functions of conservative variables. For $j = 1, 2, \ldots, N_k - 1$ it follows that

$$\beta_j = \frac{\overline{\rho}\tilde{Y}_j}{\overline{\rho}}\left\{\frac{1}{\overline{\rho}\sigma_Y}\left[\sum_{l=1}^{N_k-1}\overline{\rho}\tilde{Y}_l\left(2 - \frac{\overline{\rho}\tilde{Y}_l}{\overline{\rho}}\right) - \frac{1}{\overline{\rho}}\left(\sum_{l=1}^{N_k-1}\overline{\rho}\tilde{Y}_l\right)^2\right] - 1\right\} \tag{48}$$

and for the last species

$$\beta_{N_k} = \left\{1 - \frac{1}{\overline{\rho}}\sum_{l=1}^{N_k-1}\overline{\rho}\tilde{Y}_l\right\}\left\{\frac{1}{\overline{\rho}\sigma_Y}\left[\sum_{l=1}^{N_k-1}\overline{\rho}\tilde{Y}_l\left(2 - \frac{\overline{\rho}\tilde{Y}_l}{\overline{\rho}}\right) - \frac{1}{\overline{\rho}}\left(\sum_{l=1}^{N_k-1}\overline{\rho}\tilde{Y}_l\right)^2\right] - 1\right\} \tag{49}$$

is deduced from the normalization property. The parameters β_j are then differentiated with respect to the conservative variables to give

$$\frac{\partial \beta_j}{\partial \overline{\rho}} = -\frac{1}{\overline{\rho}}\left[2\beta_j + \tilde{Y}_j - \frac{2\tilde{Y}_j}{\sigma_Y}(1 - \tilde{Y}_{N_k}) - \delta_{jN_k}B\right], \tag{50}$$

$$\frac{\partial \beta_j}{\partial(\overline{\rho}\sigma_Y)} = -\frac{1}{\overline{\rho}\sigma_Y}(\tilde{Y}_j + \beta_j), \tag{51}$$

$$\frac{\partial \beta_j}{\partial(\overline{\rho}\tilde{Y}_k)} = \frac{2\tilde{Y}_j}{\overline{\rho}\sigma_Y}(\tilde{Y}_{N_k} - \tilde{Y}_k) + \delta_{jk}\frac{B}{\overline{\rho}} - \delta_{jN_k}\frac{B}{\overline{\rho}}, \tag{52}$$

where δ_{ij} is the Kronecker δ. Derivatives with respect to all remaining entries of variable vector $\mathbf{Q}$ (e.g., $\overline{\rho}\tilde{u}$, $\overline{\rho v}$, etc.) become zero. The corresponding derivatives of the pdf parameter B (see Eq. (19)) are obtained by summing up all N_k different derivatives of β_j:

$$\frac{\partial B}{\partial \overline{\rho}} = -\frac{1}{\overline{\rho}}\left[1 + B - \frac{2}{\sigma_Y}(1 - \tilde{Y}_{N_k})\right], \tag{53}$$

$$\frac{\partial B}{\partial(\overline{\rho}\sigma_Y)} = -\frac{1}{\overline{\rho}\sigma_Y}(1 + B), \tag{54}$$

$$\frac{\partial B}{\partial(\overline{\rho}\tilde{Y}_k)} = \frac{2}{\overline{\rho}\sigma_Y}(\tilde{Y}_{N_k} - \tilde{Y}_k). \tag{55}$$

Once more, all derivatives with respect to other elements of $\mathbf{Q}$ are zero. The next step is the derivation of terms T_1 to T_6 and P_1 to P_4 with respect to conservative variables. These terms form the species and species variance source terms. T_1 is a function of $\tilde{T}$ and I_T only and its derivative is already given in Eq. (40). T_2 depends merely on density and may be easily differentiated:

$$\frac{\partial T_2}{\partial \bar{\rho}} = \frac{T_2 m_r}{\bar{\rho}}. \tag{56}$$

Terms T_3 through T_6 are functions of $\bar{\rho}$, $\bar{\rho}\sigma_Y$, and $\bar{\rho}\tilde{Y}_i$. For their differentiation we use P_1 through P_4 (defined by Eqs. (27) and (32)),

$$\frac{\partial P_1}{\partial \mathcal{X}} = P_1 \sum_{j=1}^{N_k} \sum_{l=1}^{\nu_{jr}} \frac{1}{\beta_j + \nu_{jr} - l} \frac{\partial \beta_j}{\partial \mathcal{X}}, \tag{57}$$

$$\frac{\partial P_2}{\partial \mathcal{X}} = P_2 \frac{\partial B}{\partial \mathcal{X}} \sum_{j=1}^{m_r} \frac{1}{B + m_r - j}, \tag{58}$$

$$\frac{\partial P_3}{\partial \mathcal{X}} = \frac{\partial \beta_i}{\partial \mathcal{X}}, \tag{59}$$

$$\frac{\partial P_4}{\partial \mathcal{X}} = \frac{\partial B}{\partial \mathcal{X}}, \tag{60}$$

where $\mathcal{X}$ denotes $\bar{\rho}$, $\bar{\rho}\sigma_Y$, or $\bar{\rho}\widetilde{Y}_i$. All remaining derivatives are zero. Thus with

$$\frac{\partial T_3}{\partial \mathcal{X}} = \frac{1}{P_2}\left(\frac{\partial P_1}{\partial \mathcal{X}} - T_3 \frac{\partial P_2}{\partial \mathcal{X}}\right), \tag{61}$$

$$\frac{\partial T_4}{\partial \mathcal{X}} = \sum_{j=1}^{N_k} \frac{t_j}{M_j} \frac{\partial \beta_j}{\partial \mathcal{X}}, \tag{62}$$

$$\frac{\partial T_5}{\partial \mathcal{X}} = \frac{1}{P_4}\left(\frac{\partial \beta_i}{\partial \mathcal{X}} - T_5 \frac{\partial B}{\partial \mathcal{X}}\right), \tag{63}$$

$$\frac{\partial T_6}{\partial \mathcal{X}} = \frac{\partial T_4}{\partial \mathcal{X}}, \tag{64}$$

we now have all that is needed to apply the chain rule and obtain the elements of the source Jacobian matrix.

4.2. *Derivatives of Species Source Terms*

While the source terms $\overline{S_i}$ are functions of the temperature fluctuation intensity I_T and species variance σ_Y, the mean temperature is independent of these variables. Therefore, all mean temperature derivatives with respect to I_T and σ_Y become zero. Defining

$$A_1 = \left.\frac{\partial \overline{S_i}}{\partial \tilde{T}}\right|_{\mathbf{Q}^1 \setminus \tilde{T}} - \frac{I_T}{\tilde{T}} \left.\frac{\partial \overline{S_i}}{\partial I_T}\right|_{\mathbf{Q}^1 \setminus I_T} \tag{65}$$

and applying the chain rule, we get for the derivative

- with respect to $\bar{\rho}$

$$\left.\frac{\partial \overline{S_i}}{\partial \bar{\rho}}\right|_{\mathbf{Q}\setminus\bar{\rho}} = \underbrace{\left.\frac{\partial \overline{S_i}}{\partial \bar{\rho}}\right|_{\mathbf{Q^1}\setminus\bar{\rho}}}_{1a} + \underbrace{\left.\frac{\partial \overline{S_i}}{\partial \tilde{T}}\right|_{\mathbf{Q^1}\setminus\tilde{T}} \left.\frac{\partial \tilde{T}}{\partial \bar{\rho}}\right|_{\mathbf{Q}\setminus\bar{\rho}}}_{1b} + \underbrace{\left.\frac{\partial \overline{S_i}}{\partial I_T}\right|_{\mathbf{Q^1}\setminus I_T} \left.\frac{\partial I_T}{\partial \bar{\rho}}\right|_{\mathbf{Q}\setminus\bar{\rho}}}_{1c}, \tag{66}$$

$$1a = M_i \sum_{r=1}^{N_r} (\nu''_{ir} - \nu'_{ir}) \left[\bar{k}_{f_r} \frac{\partial}{\partial \bar{\rho}} (T_{2f} T_{3f} T_{4f}) - \bar{k}_{b_r} \frac{\partial}{\partial \bar{\rho}} (T_{2b} T_{3b} T_{4b}) \right] \tag{67}$$

$$1b = \left.\frac{\partial \overline{S_i}}{\partial \tilde{T}}\right|_{\mathbf{Q^1}\setminus\tilde{T}} \frac{1}{\bar{\rho} c_v} \left[\frac{1}{2} (\tilde{u}^2 + \tilde{v}^2) + q^2 - \tilde{e}_{N_k} \right] \tag{68}$$

$$\begin{aligned} 1c &= \left.\frac{\partial \overline{S_i}}{\partial I_T}\right|_{\mathbf{Q^1}\setminus I_T} \left[\left.\frac{\partial I_T}{\partial \rho}\right|_{\mathbf{Q^2}\setminus\rho} + \left.\frac{\partial I_T}{\partial \tilde{T}}\right|_{\mathbf{Q^2}\setminus\tilde{T}} \left.\frac{\partial \tilde{T}}{\partial \rho}\right|_{\mathbf{Q}\setminus\rho} \right] \\ &= \left.\frac{\partial \overline{S_i}}{\partial I_T}\right|_{\mathbf{Q^1}\setminus I_T} \left[\frac{I_T}{\bar{\rho}} \left(\frac{1}{2} - \frac{e_{s_{N_k}}}{e_s} \right) - \frac{I_T}{\tilde{T}} \frac{1}{\bar{\rho} c_v} \left(\frac{1}{2} (\tilde{u}^2 + \tilde{v}^2) + q^2 - \tilde{e}_{N_k} \right) \right], \end{aligned} \tag{69}$$

- with respect to $\bar{\rho}\tilde{u}$

$$\begin{aligned} \left.\frac{\partial \overline{S_i}}{\partial (\bar{\rho}\tilde{u})}\right|_{\mathbf{Q}\setminus\bar{\rho}\tilde{u}} &= \left.\frac{\partial \overline{S_i}}{\partial \tilde{T}}\right|_{\mathbf{Q^1}\setminus\tilde{T}} \left.\frac{\partial \tilde{T}}{\partial (\bar{\rho}\tilde{u})}\right|_{\mathbf{Q}\setminus\bar{\rho}\tilde{u}} + \left.\frac{\partial \overline{S_i}}{\partial I_T}\right|_{\mathbf{Q^1}\setminus I_T} \left.\frac{\partial I_T}{\partial (\bar{\rho}\tilde{u})}\right|_{\mathbf{Q}\setminus\bar{\rho}\tilde{u}} \\ &= -\frac{\tilde{u}}{\bar{\rho} c_v} A_1, \end{aligned} \tag{70}$$

- with respect to $\bar{\rho}\tilde{E}$

$$\begin{aligned} \left.\frac{\partial \overline{S_i}}{\partial (\bar{\rho}\tilde{E})}\right|_{\mathbf{Q}\setminus\bar{\rho}\tilde{E}} &= \left.\frac{\partial \overline{S_i}}{\partial \tilde{T}}\right|_{\mathbf{Q^1}\setminus\tilde{T}} \left.\frac{\partial \tilde{T}}{\partial (\bar{\rho}\tilde{E})}\right|_{\mathbf{Q}\setminus\bar{\rho}\tilde{E}} + \left.\frac{\partial \overline{S_i}}{\partial I_T}\right|_{\mathbf{Q^1}\setminus I_T} \left.\frac{\partial I_T}{\partial (\bar{\rho}\tilde{E})}\right|_{\mathbf{Q}\setminus\bar{\rho}\tilde{E}} \\ &= \frac{1}{\bar{\rho} c_v} A_1, \end{aligned} \tag{71}$$

- with respect to $\bar{\rho}q$

$$\begin{aligned} \left.\frac{\partial \overline{S_i}}{\partial (\bar{\rho} q)}\right|_{\mathbf{Q}\setminus\bar{\rho}q} &= \left.\frac{\partial \overline{S_i}}{\partial \tilde{T}}\right|_{\mathbf{Q^1}\setminus\tilde{T}} \left.\frac{\partial \tilde{T}}{\partial (\bar{\rho} q)}\right|_{\mathbf{Q}\setminus\bar{\rho}q} + \left.\frac{\partial \overline{S_i}}{\partial I_T}\right|_{\mathbf{Q^1}\setminus I_T} \left.\frac{\partial I_T}{\partial (\bar{\rho} q)}\right|_{\mathbf{Q}\setminus\bar{\rho}q} \\ &= -\frac{2q}{\bar{\rho} c_v} A_1, \end{aligned} \tag{72}$$

- with respect to $\bar{\rho}\sigma_e$

$$\left.\frac{\partial \overline{S_i}}{\partial (\bar{\rho}\sigma_e)}\right|_{\mathbf{Q}\setminus\bar{\rho}\sigma_e} = \left.\frac{\partial \overline{S_i}}{\partial I_T}\right|_{\mathbf{Q^1}\setminus I_T} \left.\frac{\partial I_T}{\partial (\bar{\rho}\sigma_e)}\right|_{\mathbf{Q}\setminus\bar{\rho}\sigma_e} = \left.\frac{\partial \overline{S_i}}{\partial I_T}\right|_{\mathbf{Q^1}\setminus I_T} \frac{1}{2} \frac{I_T}{\bar{\rho}\sigma_e}, \tag{73}$$

- with respect to $\bar{\rho}\sigma_Y$

$$\left.\frac{\partial \overline{S_i}}{\partial (\bar{\rho}\sigma_Y)}\right|_{\mathbf{Q}\setminus\rho\sigma_Y} = M_i \sum_{r=1}^{N_r} (\nu''_{ir} - \nu'_{ir}) \left[\bar{k}_{f_r} T_{2f} \frac{\partial}{\partial (\bar{\rho}\sigma_Y)} (T_{3f} T_{4f}) - \bar{k}_{b_r} T_{2b} \frac{\partial}{\partial (\bar{\rho}\sigma_Y)} (T_{3b} T_{4b}) \right], \tag{74}$$

- with respect to $\overline{\rho}\tilde{Y}_k$

$$\left.\frac{\partial \overline{S_i}}{\partial(\overline{\rho}\tilde{Y}_k)}\right|_{\mathbf{Q}\setminus\overline{\rho}\tilde{Y}_k} = \left.\frac{\partial \overline{S_i}}{\partial \tilde{T}}\right|_{\mathbf{Q}^1\setminus\tilde{T}} \left.\frac{\partial \tilde{T}}{\partial(\overline{\rho}\tilde{Y}_k)}\right|_{\mathbf{Q}\setminus\overline{\rho}\tilde{Y}_k} + \left.\frac{\partial \overline{S_i}}{\partial I_T}\right|_{\mathbf{Q}^1\setminus I_T} \left.\frac{\partial I_T}{\partial(\overline{\rho}\tilde{Y}_k)}\right|_{\mathbf{Q}\setminus\overline{\rho}\tilde{Y}_k} + \left.\frac{\partial \overline{S_i}}{\partial(\overline{\rho}\tilde{Y}_k)}\right|_{\mathbf{Q}^1\setminus\overline{\rho}\tilde{Y}_k}$$

$$= -\frac{\tilde{e}_k - \tilde{e}_{N_k}}{\overline{\rho} c_v} A_1 - \left.\frac{\partial \overline{S_i}}{\partial I_T}\right|_{\mathbf{Q}^1\setminus I_T} \frac{I_T}{\overline{\rho} e_s}\left(\tilde{e}_{s_k} - \tilde{e}_{s_{N_k}}\right) + M_i \sum_{r=1}^{N_r} (\nu''_{ir} - \nu'_{ir})$$

$$\times \left[\overline{k}_{f_r} T_{2f} \frac{\partial}{\partial(\overline{\rho}\tilde{Y}_k)}(T_{3f} T_{4f}) - \overline{k}_{b_r} T_{2b} \frac{\partial}{\partial(\overline{\rho}\tilde{Y}_k)}(T_{3b} T_{4b})\right], \tag{75}$$

where e and e_s denote the specific energy and the sensible specific energy of the gas mixture, and an additional index indicates a particular species. The averaged species source terms are independent of the turbulence variable ω, so that this derivative becomes zero.

4.3. *PDF Source Terms Formed by Spatial Derivatives*

Like the conservation equations of any available two-equation turbulence model, the pdf equations contain production terms that are formed by spatial derivatives of fluid variables. In the present case, S_{e1} and S_{e2} in Eq. (14) as well as S_{Y1} in Eq. (21) represent such derivatives that are calculated by central differences. Thus the corresponding source Jacobian would include entries at four neighboring volumes. To treat these terms in the implicit part of numerical schemes is computationally expensive. Sinha and Candler [30] included corresponding expressions of a k–ϵ turbulence model in the implicit operator but usually such terms are treated explicitly. For the species variance equation the situation is still more complicated owing to the sum over all species derivatives. Fortunately, an implicit treatment of these parts was found to be less critical and is therefore not attempted in the present paper. For all investigated test cases machine accuracy could be reached without linearizing these terms.

4.4. *Derivatives of PDF Terms*

All source terms in the pdf equations are located on the right hand sides of Eqs. (14) and (21). As mentioned in the previous paragraph, contributions containing spatial derivatives are kept constant. Thus, with the exception of the last term in the species variance equation, all derivatives can be easily obtained if the fluid properties ($\hat{\gamma}$, c_v, etc.) are treated as frozen. However, the most cumbersome term is the last one appearing in Eq. (21). The use of a single instead of N_k species variance equations is paid for by the sum

$$S_s = \sum_{i=1}^{N_k} \overline{Y_i'' S_i} = \sum_{i=1}^{N_k} (\overline{Y_i S_i} - \tilde{Y}_i \overline{S_i}), \tag{76}$$

which is expensive to calculate and complex to linearize. While the product $\tilde{Y}_i \overline{S_i}$ and all its derivatives are already known, $\overline{Y_i S_i}$ has to be calculated according to Eq. (31) and the corresponding derivatives follow as

$$\frac{\partial S_s}{\partial \overline{\rho}} = \sum_{i=1}^{N_k} \left(\frac{\partial(\overline{Y_i S_i})}{\partial \overline{\rho}} + \frac{\tilde{Y}_i}{\overline{\rho}} \overline{S_i} - \tilde{Y}_i \frac{\partial \overline{S_i}}{\partial \overline{\rho}} \right), \tag{77}$$

$$\frac{\partial S_s}{\partial(\overline{\rho}\tilde{Y}_j)} = \sum_{i=1}^{N_k} \left(\frac{\partial(\overline{Y_i S_i})}{\partial(\overline{\rho}\tilde{Y}_j)} - \tilde{Y}_i \frac{\partial \overline{S_i}}{\partial(\overline{\rho}\tilde{Y}_j)} \right) - \frac{\overline{S_j}}{\overline{\rho}}, \tag{78}$$

for $j = 1, 2, \ldots, N_k - 1$, and

$$\frac{\partial S_s}{\partial \chi} = \sum_{i=1}^{N_k} \left(\frac{\partial(\overline{Y_i S_i})}{\partial \chi} - \tilde{Y}_i \frac{\partial \overline{S_i}}{\partial \chi} \right), \tag{79}$$

where χ represents any of the remaining conservative variables of $\mathbf{Q}$. Finally, derivatives of $\overline{Y_i S_i}$ remain to be formed, which requires some mathematics. In principle, this procedure is similar to the derivation of the mean species production rates. Despite the complexity of these derivatives, many terms involved are already known (e.g., T_1 to T_4) and much CPU time can be saved by careful programming. This time, we only present the results that again are obtained by applying the chain rule for partial derivatives. Defining

$$B_1 = \frac{\partial(\overline{Y_i S_i})}{\partial \tilde{T}}\bigg|_{\mathbf{Q}^1 \setminus \tilde{T}} - \frac{I_T}{\tilde{T}} \frac{\partial(\overline{Y_i S_i})}{\partial I_T}\bigg|_{\mathbf{Q}^1 \setminus I_T} \tag{80}$$

we get for the derivative

- with respect to $\bar{\rho}$

$$\frac{\partial(\overline{Y_i S_i})}{\partial \bar{\rho}}\bigg|_{\mathbf{Q}\setminus\bar{\rho}} = \underbrace{\frac{\partial(\overline{Y_i S_i})}{\partial \bar{\rho}}\bigg|_{\mathbf{Q}^1\setminus\bar{\rho}}}_{\text{2a}} + \underbrace{\frac{\partial(\overline{Y_i S_i})}{\partial \tilde{T}}\bigg|_{\mathbf{Q}^1\setminus\tilde{T}} \frac{\partial \tilde{T}}{\partial \bar{\rho}}\bigg|_{\mathbf{Q}\setminus\bar{\rho}}}_{\text{2b}} + \underbrace{\frac{\partial(\overline{Y_i S_i})}{\partial I_T}\bigg|_{\mathbf{Q}^1\setminus I_T} \frac{\partial I_T}{\partial \bar{\rho}}\bigg|_{\mathbf{Q}\setminus\bar{\rho}}}_{\text{2c}} \tag{81}$$

$$\text{2a} = M_i \sum_{r=1}^{N_r} (\nu''_{ir} - \nu'_{ir}) \left[\bar{k}_{f_r} \frac{\partial}{\partial \bar{\rho}} (T_{2f} T_{3f} T_{5f} T_{6f}) - \bar{k}_{b_r} \frac{\partial}{\partial \bar{\rho}} (T_{2b} T_{3b} T_{5b} T_{6b}) \right], \tag{82}$$

$$\text{2b} = \frac{\partial(\overline{Y_i S_i})}{\partial \tilde{T}}\bigg|_{\mathbf{Q}^1\setminus\tilde{T}} \frac{1}{\bar{\rho} c_v} \left[\frac{1}{2}(\tilde{u}^2 + \tilde{v}^2) + q^2 - \tilde{e}_{N_k} \right], \tag{83}$$

$$\text{2c} = \frac{\partial(\overline{Y_i S_i})}{\partial I_T}\bigg|_{\mathbf{Q}^1\setminus I_T} \left[\frac{I_T}{\bar{\rho}} \left(\frac{1}{2} - \frac{e_{s_{N_k}}}{e_s} \right) - \frac{I_T}{\tilde{T}} \frac{1}{\bar{\rho} c_v} \left(\frac{1}{2}(\tilde{u}^2 + \tilde{v}^2) + q^2 - \tilde{e}_{N_k} \right) \right], \tag{84}$$

- with respect to $\bar{\rho}\tilde{u}$

$$\frac{\partial(\overline{Y_i S_i})}{\partial(\bar{\rho}\tilde{u})}\bigg|_{\mathbf{Q}\setminus\bar{\rho}\tilde{u}} = -\frac{\tilde{u}}{\bar{\rho} c_v} B_1, \tag{85}$$

- with respect to $\bar{\rho}\tilde{E}$

$$\frac{\partial(\overline{Y_i S_i})}{\partial(\bar{\rho}\tilde{E})}\bigg|_{\mathbf{Q}\setminus\bar{\rho}\tilde{E}} = \frac{1}{\bar{\rho} c_v} B_1, \tag{86}$$

- with respect to $\bar{\rho} q$

$$\frac{\partial(\overline{Y_i S_i})}{\partial(\bar{\rho} q)}\bigg|_{\mathbf{Q}\setminus\bar{\rho}q} = -\frac{2q}{\bar{\rho} c_v} B_1, \tag{87}$$

- with respect to $\bar{\rho}\sigma_e$

$$\frac{\partial(\overline{Y_i S_i})}{\partial(\bar{\rho}\sigma_e)}\bigg|_{\mathbf{Q}\setminus\rho\sigma_e} = \frac{\partial(\overline{Y_i S_i})}{\partial I_T}\bigg|_{\mathbf{Q}^1\setminus I_T} \frac{1}{2} \frac{I_T}{\bar{\rho}\sigma_e}, \tag{88}$$

- with respect to $\bar{\rho}\sigma_Y$

$$\left.\frac{\partial(\overline{Y_i S_i})}{\partial(\bar{\rho}\sigma_Y)}\right|_{\mathbf{Q}\setminus\rho\sigma_Y} = M_i \sum_{r=1}^{N_r}(\nu''_{ir} - \nu'_{ir})\left[\bar{k}_{f_r} T_{2f} \frac{\partial}{\partial(\bar{\rho}\sigma_Y)}(T_{3f} T_{5f} T_{6f}) - \bar{k}_{b_r} T_{2b} \frac{\partial}{\partial(\bar{\rho}\sigma_Y)}(T_{3b} T_{5b} T_{6b})\right], \tag{89}$$

- with respect to $\bar{\rho}\tilde{Y}_k$

$$\left.\frac{\partial(\overline{Y_i S_i})}{\partial(\bar{\rho}\tilde{Y}_k)}\right|_{\mathbf{Q}\setminus\bar{\rho}\tilde{Y}_k} = -\frac{\tilde{e}_k - \tilde{e}_{N_k}}{\bar{\rho} c_v} B_1 - \left.\frac{\partial\overline{Y_i S_i}}{\partial I_T}\right|_{\mathbf{Q}^1\setminus I_T} \frac{I_T}{\bar{\rho}\bar{e}_s}\left(\tilde{e}_{s_k} - \tilde{e}_{s_{N_k}}\right) + M_i \sum_{r=1}^{N_r}(\nu''_{ir} - \nu'_{ir}) \times \left[\bar{k}_{f_r} T_{2f} \frac{\partial}{\partial(\bar{\rho}\tilde{Y}_k)}(T_{3f} T_{6f}) - \bar{k}_{b_r} T_{2b} \frac{\partial}{\partial(\bar{\rho}\tilde{Y}_k)}(T_{3b} T_{6b})\right], \tag{90}$$

while the derivative with respect to $\rho\omega$ becomes zero.

5. THE MULTIGRID METHOD

An efficient numerical algorithm is a basic requirement for the engineering use of CFD in combustor design. In principle, multigrid methods can be applied for convergence acceleration in conjunction with any iterative solver that is able to efficiently damp out high-frequency error components. While excellent results or even textbook multigrid efficiency may be achieved for subsonic or transonic flows [12, 13], problems arise in cases of

- strong shock waves,
- highly stretched grids,
- turbulence, and
- finite rate chemistry.

This paper focusses on the last point, chemical source terms appearing in species and pdf transport equations. The efficiency of multigrid methods results from the fact that low-frequency error components are damped out more efficiently on coarser grid levels. A second advantage is the possibility of using larger time steps on coarse grids. In dealing with chemically reacting flows, problems arise from strongly nonlinear source terms. In the case of a full coarsening multigrid strategy, coarse grid variables are linearly calculated from corresponding fine grid values. It is obvious that a recalculation of strongly nonlinear functions with linearly averaged variables causes large differences in these terms at different grid levels. In most cases the consequence is failure of the multigrid method. Moreover, chemistry is a local phenomenon and, hence, the basic features of multigrid methods (damping out spatial low-frequency errors) do not work. Nevertheless, convergence acceleration is possible. Combustion is mostly limited to narrow regions of the flow field and even if the full potential of multigrid methods cannot be used in the main reaction zone, there still is a strong influence in the remaining flow field. To allow the use of large time steps at coarse grid levels, chemistry is treated fully coupled with fluid motion as explained above.

A full coarsening V-cycle multigrid method based on the full approximation storage (FAS) scheme of Brandt [10] is considered in the present paper. The implicit version for approximately factored schemes was first presented by Jameson and Yoon [11]. Coarse grids

are formed by eliminating every other grid line of the previous finer mesh. The calculation is initialized by a nested iteration approach. Prolongation of corrections from coarse to fine grids is performed by bilinear interpolation. Further details of the multigrid method employed here may be found in Ref. [9]. Therefore, only modifications of the restriction operator which are necessary to enable convergence in case of finite-rate chemistry and pdf modeling are explained.

5.1. *Restriction*

Local damping of the restricted residual error is used in the present paper to enable convergence of the multigrid method in case of strong shock waves and finite-rate chemistry. Such a damping is associated with a loss of information at coarser grid levels leading to a reduction in convergence acceleration. On the other hand, combustion is often limited to small spatial regions and the full multigrid method keeps working outside of main reaction zones. An additional advantage of this method is its simplicity. This procedure has similarity with the damping at shock waves and is easy to include in any multigrid solver. The sensor proposed in Ref. [9] for the simulation of finite-rate chemistry is extended here to include turbulence chemistry interaction.

The following transfer operators are used for the applied full coarsening cell-centered finite-volume method.

- $I_{k\mapsto k+1}$ for restriction of flow variables [11],

$$I_{k\mapsto k+1}\mathbf{Q}^k = \frac{1}{\Omega^{k+1}}\sum_{l=1}^{4}\Omega_l^k\mathbf{Q}_l^k, \tag{91}$$

where Ω denotes the corresponding cell area at grid level k. Four fine grid volumes are collected forming one coarse grid volume.

- $\bar{I}_{k\mapsto k+1}$ for restriction of residuals or residual errors [9],

$$\bar{I}_{k\mapsto k+1}\mathbf{R}^k = \sum_{l=1}^{4}\mathbf{R}_l^k\max\left[0, \min\left(1-\kappa_l^k, 1-\gamma_l^k\right)\right]. \tag{92}$$

Instead of simply adding four fine grid residuals $\mathbf{R}$, the transfer is damped by parameter κ_l^k near shock waves and by γ_l^k in regions of high chemical activity. A similar damping has been introduced by Radespiel and Swanson [31] for the simulation of shock waves in hypersonic, nonreactive flows. To locate shock waves within the flow field, a blend between the standard pressure-based sensor [32] and a sensor with TVD properties [33] is employed,

$$\nu_{i,j}^{\xi} = \frac{|p_{i+1,j} - 2p_{i,j} + p_{i-1,j}|}{(1-\chi)(|p_{i+1,j} - p_{i,j}| + |p_{i,j} - p_{i-1,j}|) + \chi(p_{i+1,j} + 2p_{i,j} + p_{i-1,j})}, \tag{93}$$

which is given here for the ξ-direction. χ takes values between 0.8 and 1 in the following simulations. The damping parameter κ^k is formed by the maximum of neighboring values of ν,

$$\kappa^k = C^k\max\left(\nu_{i,j}^{\xi}, \nu_{i-1,j}^{\xi}, \nu_{i+1,j}^{\xi}, \nu_{i,j}^{\eta}, \nu_{i,j-1}^{\eta}, \nu_{i,j+1}^{\eta}\right). \tag{94}$$

By constants C^k the damping factors can be adjusted to the decreasing smoothness of

the pressure distribution on successively coarser grids. To locate regions of high chemical activity we introduce an additional sensor,

$$\gamma^k = B^k \left(\frac{1}{N_k} \sum_{i=1}^{N_k} \frac{\left|S_i^k\right|}{S_{i,\max}^k + \epsilon} \right)^{\alpha}. \tag{95}$$

$S_{i,\max}^k$ represents the maximum absolute production rate of species i within the flow field, k denotes the grid level, B^k is a grid-level-dependent constant ($0 \leq B^k \leq 1$), and ϵ is a small number to avoid division by zero. It was found to be advantageous that all N_k individual species production rates contribute to this sensor ($0 \leq \gamma \leq 1$). An exponent α of 0.3 ensures a smooth distribution and worked satisfactorily for the test cases described later.

Because combustion is usually associated with strong gradients in density, a density-based sensor similar to Eq. (93) can alternatively be used to reduce coarse grid residuals.

In addition to damping the transferred residual error, the coarse grid time step is reduced at the beginning of the iteration process. The standard time step Δt_s is replaced by

$$\Delta t^k = \Delta t_s^k \max\left[\epsilon, \min\left(1 - \kappa_l^k, 1 - \gamma_l^k\right)\right] \quad \text{for } k > 1, \tag{96}$$

where ϵ is a limit that is chosen to be 0.01.

The described damping of restricted residual errors was found to be essential owing to strong nonlinearities in the chemical source terms. However, these source terms are pure functions of local values. Another difficulty arises if nonlinear source terms include spatial derivatives. This is the case for the production of turbulent kinetic energy [9, 21] and for S_{e1}, S_{e2}, and S_{Y1} in the pdf transport equations (see Eqs. (14) and (21)). In discretized form, these terms require neighboring values. It is obvious that a recalculation of such terms at different grid levels causes strong differences that can lead to divergence of the multigrid solver. Therefore, we adopted a simple and stable method used before for the turbulence equtions [34]. The main production terms of variance in energy and the sum of species fluctuations, S_{e1} and S_{Y1}, respectively, are calculated on the finest grid only and passed on to coarser grid levels by

$$\begin{aligned} S_{e1}^{k+1} &= I_{k \mapsto k+1}\, S_{e1}^k, \\ S_{Y1}^{k+1} &= I_{k \mapsto k+1}\, S_{Y1}^k, \end{aligned} \tag{97}$$

where they are kept constant. Such a simple freezing of strongly nonlinear parts allows the multigrid method to converge. For simplicity the same treatment is used for S_{e2}, the divergence of the velocity field. Both treatments,

- freezing of terms formed by spatial derivatives and
- damping of the restricted residual errors,

are performed simultaneously. This is necessary because high production rates of species and pdf variables often are located in different parts of the flow field.

6. RESULTS AND DISCUSSION

Numerical tests are performed in order to evaluate robustness of the implicit treatment of pdf source terms as well as efficiency of the proposed multigrid algorithm. A nested

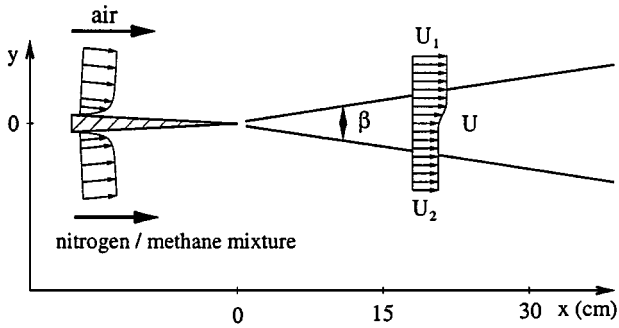

FIG. 2. Geometry for planar reactive shear flow.

iteration process using four grid levels serves to initialize the flow field on the finest grid. All computations are started by fixing the inflow properties to the interior of the domain. The first simulation is a theoretical test case for which no experimental data are available. The purpose of this simulation is to investigate the influence of the assumed pdf closure on ignition delay and to use the multigrid method for a lifted flame simulation. The second test case consists of an attached supersonic diffusion flame and in addition to convergence histories, species profiles are compared with experimental results.

6.1. *Planar Methane Diffusion Flame*

A two-dimensional, high-speed reacting mixing layer serves to investigate convergence properties and the influence of the assumed pdf approach on ignition delay. This simulation resembles those of Refs. [24] and [35], with the exception that methane is used instead of hydrogen in the present case. The model problem corresponds to a supersonic shear flow over a splitter plate with 4° angle (see Fig. 2). Precalculated, fully turbulent inlet profiles with $\delta = 0.5$-cm boundary layer thickness are specified for both streams. Table III summarizes pertinent inflow conditions of the upper air and the lower methane–nitrogen stream. A constant free-stream temperature fluctuation intensity of $I_T = \sqrt{\sigma_T}/\tilde{T} = 0.15$ is chosen at the inlet and the species fluctuation intensity

$$I_Y = \frac{\sigma_Y}{\sum_{m=1}^{N_k} \tilde{Y}_m (1 - \tilde{Y}_m)} \tag{98}$$

TABLE III
Inflow Conditions for Reactive Shear Flow

	Air stream	CH_4/N_2 stream
p (bar)	1.5	1.5
u (m/s)	1800	2300
T (K)	2000	2000
Y_{CH_4}	0	0.4
Y_{N_2}	0.7664	0.6
Y_{O_2}	0.2336	0
I_T	0.15	0.15
I_Y	0.002	0.002

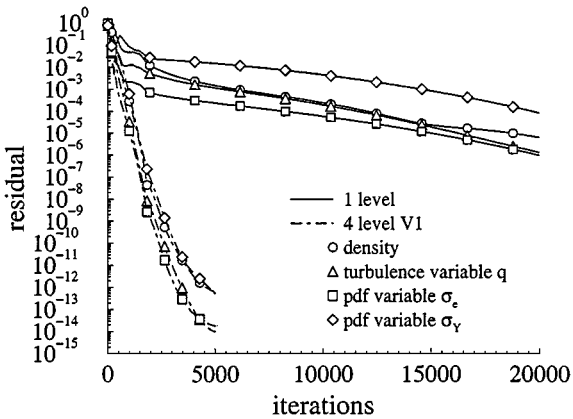

FIG. 3. Convergence histories with and without the multigrid technique versus the number of multigrid cycles.

takes a value of 0.002. This flow is characterized by its high inflow temperatures that, in the case of hydrogen, cause ignition directly at the tip of the splitter plate [9, 24]. However, a lifted flame develops if methane serves as fuel (see Fig. 5). A 58-step 17-species finite-rate reaction model [19] is employed for methane–air combustion. The simulation starts 4 cm upstream of the tip discretizing the domain by a two-block grid with 128×64 volumes each. Due to the requirements of the turbulence model and for resolution of important flow characteristics, the grid is highly clustered near solid walls, at the tip of the splitter plate, and in the combustion zone, resulting in cell aspect ratios of up to 2200. All y^+-values of near-wall-cell centers are smaller than 0.25.

Figures 3 and 4 display convergence behaviors of the calculations. Plotted are the averaged absolute normalized residuals of density $\bar{\rho}$, turbulence variable q, and pdf variables σ_e and σ_Y versus the number of multigrid cylces and work units, respectively. One work unit is defined as the computational time necessary for one fine grid iteration. It may be seen that all residuals of the four-level multigrid calculation (V1 = V-cycle with 1 coarse grid iteration) converge at about the same rate. This is an advantage if all conservation equations are treated with the multigrid technique. All residuals reach machine accuracy in about 5000 iterations.

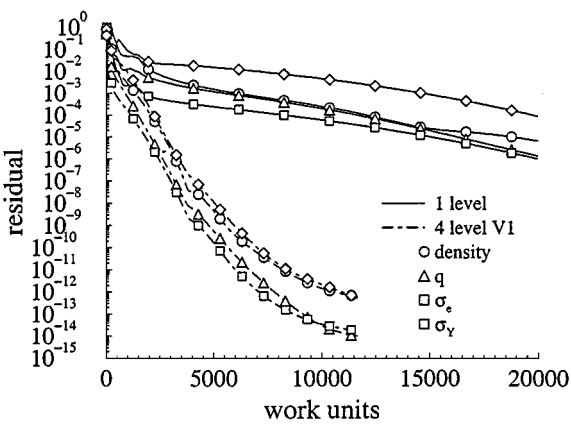

FIG. 4. Convergence histories with and without the multigrid technique versus the number of work units.

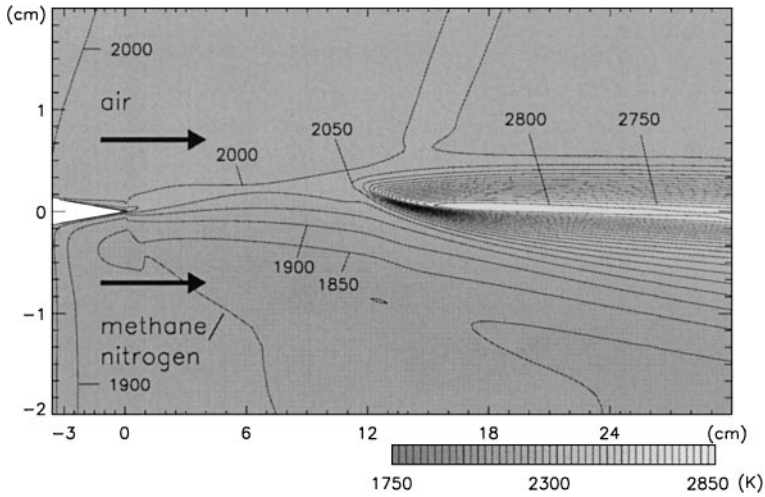

FIG. 5. Calculated temperature contours (K, $\Delta = 50$ K) with assumed pdf closure.

Because the computations are performed on a vector computer (NEC–SX4) using a fully vectorized code, reductions achieved in CPU time are smaller than the theoretically possible values, a consequence of shorter vector lengths on coarse grids reducing the performance of the code. Nevertheless, the convergence improvement relative to the single grid iteration is at least threefold. It should also be noted that the performance of simulations of detached flames using the multigrid method still exhibits strong grid size and test case dependence. If the difference in ignition delay at the different grid levels is too large, the multigrid method usually fails.

Figure 5 shows calculated temperature contours, indicating regions of heat release by combustion. These results are obtained with the assumed pdf approach. The same simulation without pdf modeling did not ignite within the computational domain. In addition, a strong dependence of ignition on the reaction mechanism is observed. In summary, the most obvious feature of the assumed pdf closure is a significant reduction in ignition delay caused by some strongly increased mean reaction rates of chain initiating reactions due to temperature fluctuations. The distribution of temperature fluctuation intensity I_T is given in Fig. 6. The relatively high free-stream inflow values for I_T of 0.15 decrease in the boundary layer approaching the splitter plate. The main production of energy variance results from gradients in energy, which in turn result from both temperature and species gradients. Because a uniform inflow temperature was assumed, energy gradients are mainly caused by species gradients upstream of the ignition point. However, gradients in species mass fractions are relatively small owing to high nitrogen mass fractions in both streams (0.6 and 0.7664). In addition, because of high inflow values the increase in temperature and thus the temperature gradients are low, too. Both effects limit the production of energy variance. After a decrease in I_T caused by the splitter plate, values increase again directly at the tip of the plate and in the main reaction zone.

Figure 7 displays the distribution of the sum of species variances σ_Y. As before, main production results from gradients in mean species mass fractions. High production rates and high values of σ_Y are located in the shear layer between both streams. Ignition and combustion cause a strong decrease in σ_Y. This effect has also been observed by Baurle

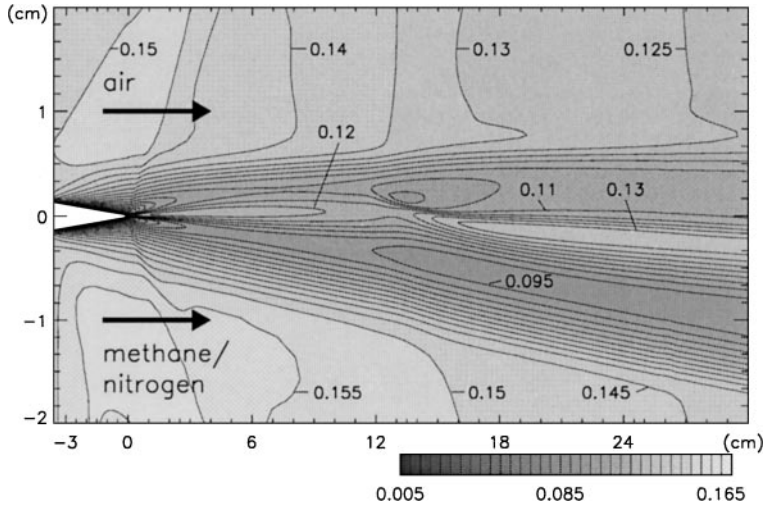

FIG. 6. Calculated contours of temperature fluctuation intensity I_T ($\Delta = 0.005$).

et al. [3] for a different test case but does not agree in its strength with experimental data. Inaccurate modeling assumptions in the σ_Y conservation equation may be responsible for this behaviour.

6.2. *Axisymmetric Shear Flow*

The second test case considered corresponds to an experiment of Evans *et al*. [36]. Figure 8 illustrates axisymmetric hydrogen injection into a preheated vitiated air stream. The inner radius of the tube is 0.326 cm; the outer one is 0.476 cm. A three-block grid is chosen to resolve the lip thickness at the end of the injector. The grid contains 136×72, 112×48, and 136×48 volumes to simulate the upper half of the symmetric problem. The calculation

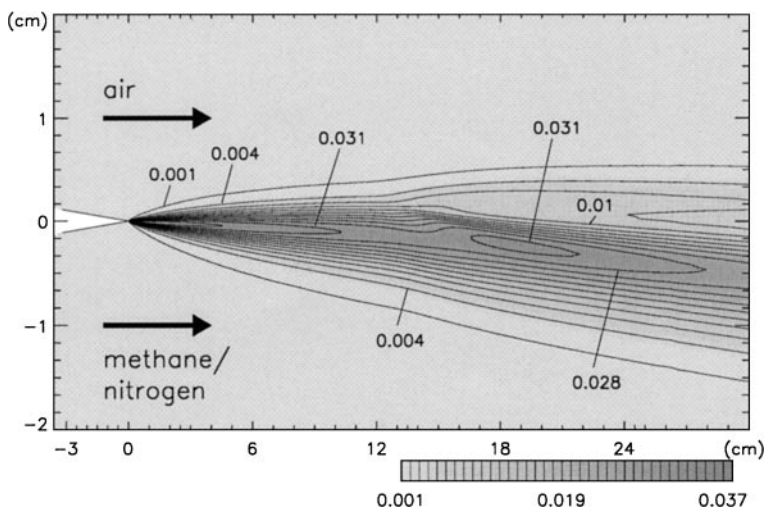

FIG. 7. Calculated contours of the sum of species variances σ_Y ($\Delta = 0.003$).

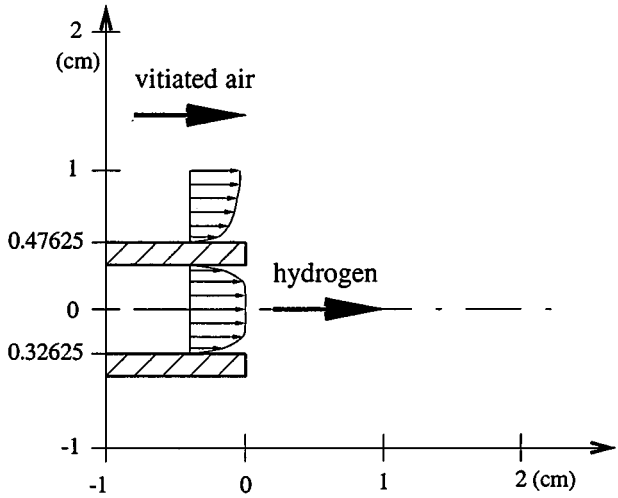

FIG. 8. Geometry (cm) for the Evans *et al.* [36] axisymmetric combustion experiment.

starts at $x = -0.33$ cm (see Fig. 12), thus simulating the inner and outer boundary layers at the tube surfaces. Precalculated, fully turbulent boundary layer profiles are specified as inflow conditions. The computational grid is highly clustered near solid walls as well as in the recirculation zone at the end of the tube. At solid walls, the minimum radial spacing amounts to 1×10^{-6} m, fine enough to ensure y^+-values smaller than 0.8 for the converged solution. The highest cell aspect ratio is about 500. The inflow conditions of the pure hydrogen and the vitiated air are summarized in Table IV. Unfortunately, no information is available about inflow boundary layer thicknesses for this experiment. This is a critical point because the results were found to be sensitive to the choice of these values. Inflow free-stream temperature fluctuation intensity and species fluctuation intensity are assigned values of 0.15 and 0.005, respectively. Both calculations (with and without the assumed pdf approach) result in an attached flame as observed in the experiment. This is due to the high temperature of the vitiated air heated by precombustion.

Figures 9 and 10 show convergence histories of the pdf simulation with and without multigrid technique versus the number of multigrid cycles and work units, respectively.

TABLE IV
Inflow Conditions for Axisymmetric Combustion Experiment of Evans *et al.* [36]

	Hydrogen jet	Vitiated air stream
p (bar)	1	1
u (m/s)	2432	1510
T (K)	251	1495
Ma	2	1.9
Y_{H_2}	1	0
Y_{H_2O}	0	0.281
Y_{N_2}	0	0.478
Y_{O_2}	0	0.241

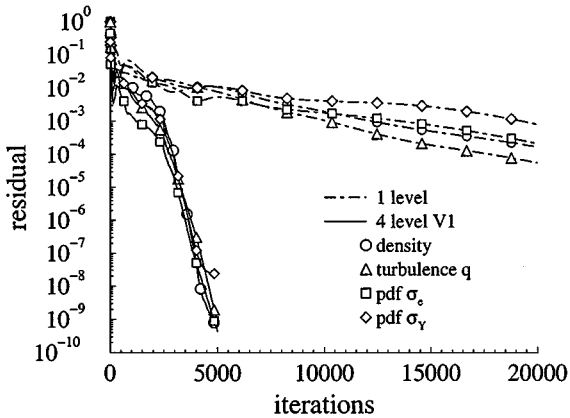

FIG. 9. Convergence histories with and without the multigrid technique for pdf simulations versus the number of multigrid cycles.

Unlike in the previous case, the coarse grid time step had to be reduced at the beginning of the iteration. Again a similar convergence behaviour is obtained for all variables by treating all conservation equations with the multigrid method. Due to the reduced coarse grid time step at the beginning, the gain from the multigrid technique turns out to be smaller than before. However, there is still a strong reduction in necessary CPU time. Figure 11 shows a comparison between simulations with and without pdf modeling. All parameters of these calculations as CFL number, restriction coefficients, and coarse-grid time-step limitation are the same. Plotted are 1- and 4-level residuals of density and turbulence variable q versus the number of multigrid cycles. Calculations with and without pdf modeling show nearly identical convergence histories. This feature demonstrates that the basic properties of the LU-SGS algorithm are maintained with pdf modeling. However, the computational effort for solving two additional equations and for the implicit treatment of averaged production rates nearly doubles the CPU time per iteration. Since the differences between calculations with and without pdf modeling are small for this test case, only contour plots with pdf modeling are presented. Figure 12 shows the calculated temperature to illustrate some global features

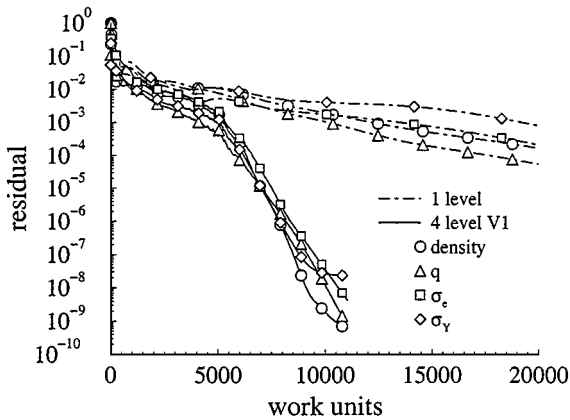

FIG. 10. Convergence histories with and without the multigrid technique for pdf simulations versus the number of work units.

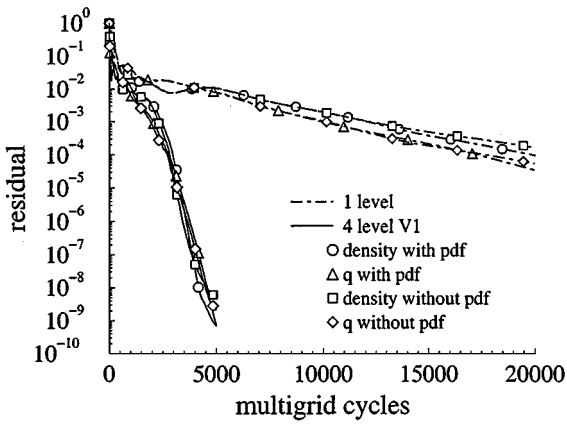

FIG. 11. Convergence histories with and without pdf modeling for 1 and 4 level simulations.

of the flow field. The highest temperature is 2342 K for the calculation with assumed pdf closure versus 2255 K with laminar chemistry. The temperature fluctuation intensity and the sum of species variances are displayed in Figs. 13 and 14. In comparison with the previous test case, a much stronger production is observed for both quantities. Reasons are the extreme temperature (and therefore energy) and species mass fraction gradients between both streams. Thus, main production is located in the shear layer directly downstream from the tube. Maximum values of I_T and σ_Y are 0.54 and 0.176, respectively. Despite these high values in variance, the effect of the pdf approach on species concentration profiles is relatively small. Species mass fraction profiles have been measured at four different streamwise locations ($x/D = 8.26$, 15.5, 21.7, and 27.9; diameter of the outer tube $D =$ 0.9525 cm). Figure 15 gives a comparison between measured and calculated profiles for $x/D = 21.7$. These graphs include calculations with and without assumed pdf modeling. As in the calculation of Edwards [16], the computed reaction zone is much thinner than that in the experiment. The use of assumed pdfs did not change that fact. However, the computational results are similar to those achieved by Baurle [26]. The overall agreement is satisfactory, especially if some uncertainty in the experiment and inexactness in the boundary conditions are taken into account.

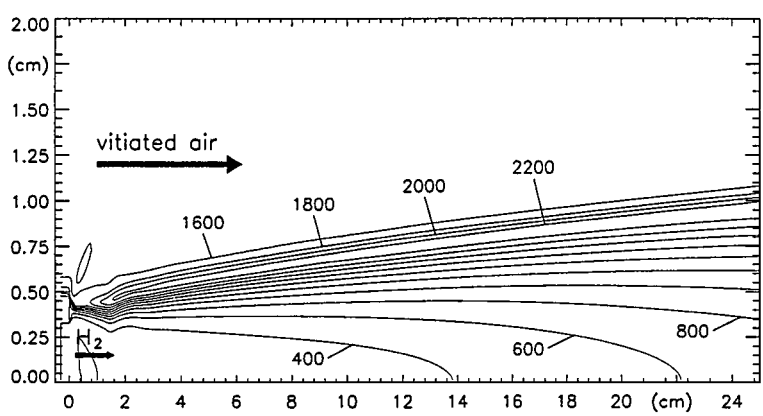

FIG. 12. Calculated temperature contours (K, $\Delta = 200$ K) for the experiment of Evans *et al.* [36].

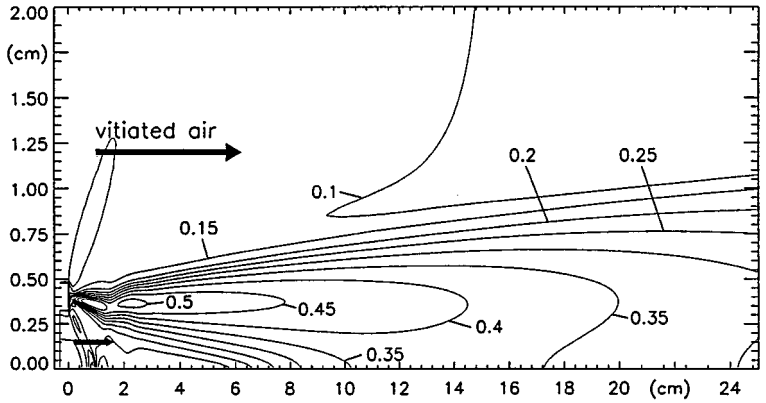

FIG. 13. Calculated temperature fluctuation intensity contours ($\Delta = 0.05$).

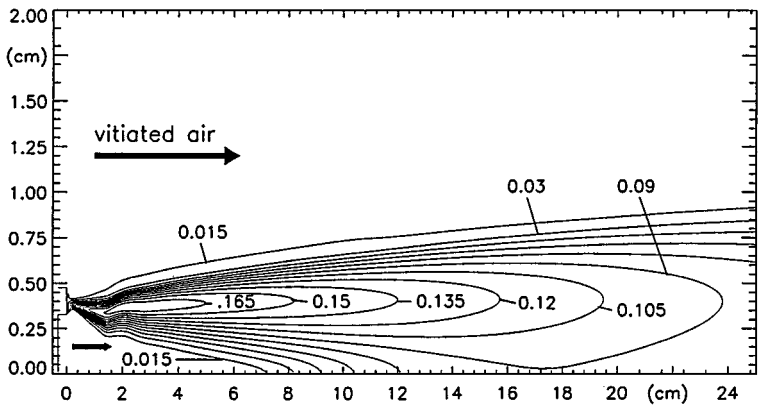

FIG. 14. Calculated sum of species variances contours ($\Delta = 0.015$).

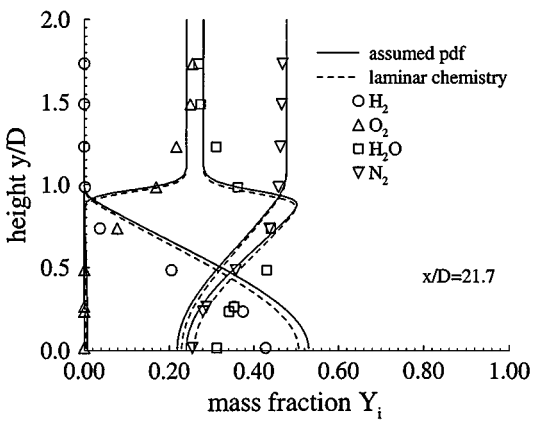

FIG. 15. Calculated and measured profiles of mass fractions at $x/D = 27.9$.

7. CONCLUSIONS

A presumed pdf approach has successfully been used to include effects of turbulent fluctuations on chemical production rates. The pdfs assumed are a Gaussian distribution for temperature and a multivariate β pdf model for species fluctuations. An analytically formed source Jacobian is presented. The implicit treatment of chemistry has maintained the good stability and convergence properties of the LU-SGS algorithm. The greatest effect of the assumed pdf closure observed was a significant reduction in ignition delay. An implicit multigrid method is used for convergence acceleration of all conservation equations. Local damping of restricted residual errors allows convergence in the case of finite-rate chemistry and pdf closure. A strong reduction in CPU time has been demonstrated for test cases with methane and hydrogen combustion. While the proposed technique achieves good results for attached flames, multigrid convergence acceleration for lifted flames is still strongly grid size and test case dependent.

ACKNOWLEDGMENTS

We thank the Deutsche Forschungsgemeinschaft (DFG) for the financial support of this work within the Collaborative Research Center SFB 259 at the University of Stuttgart.

REFERENCES

1. S. B. Pope, PDF methods for turbulent reactive flows., *Prog. Energy Combust. Sci.* **11**, 119 (1985).
2. A. T. Hsu, Y.-L. P. Tsai, and M. S. Raju, Probability density function approach for compressible turbulent reacting flows, *AIAA J.* **32**, 1407 (1994).
3. R. A. Baurle, G. A. Alexopoulos, and H. A. Hassan, Assumed joint probability density function approach for supersonic turbulent combustion, *J. Propul. Power* **10**, 473 (1994).
4. R. A. Baurle, G. A. Alexopoulos, and H. A. Hassan, *Analysis of Supersonic Combustors with Swept Ramp Injectors*, AIAA Paper 95-2413 (AIAA Press, Washington, DC, 1995).
5. H. Möbus, P. Gerlinger, and D. Brüggemann, Comparison of Eulerian and Lagrangian Monte Carlo PDF methods for turbulent diffusion flames, *Combust. Flame* **134**(3), 519 (2001).
6. F. C. Lockwood and A. S. Naguib, The prediction of the fluctuations in the properties of free, round-jet, turbulent diffusion flames, *Combust. Flame* **24**, 109 (1975).
7. S. S. Girimaji, Assumed β-pdf model for turbulent mixing: Validation and extension to multiple scalar mixing, *Combust. Sci. Technol.* **78**, 177 (1991).
8. S. Eberhardt and A. Imlay, *A Diagonal Implicit Scheme for Computing Flows with Finite-Rate Chemistry*, AIAA Paper 90-1577 (AIAA Press, Washington, DC, 1990).
9. P. Gerlinger, P. Stoll, and D. Brüggemann, An implicit multigrid method for the simulation of chemically reacting flows, *J. Comput. Phys.* **146**, 322 (1998).
10. A. Brandt, Multi-level adaptive solutions to boundary-value problems, *Math. Comput.* **31**, 333 (1977).
11. A. Jameson and S. Yoon, Lower-upper implicit schemes with multiple grids for the Euler equations, *AIAA J.* **25**, 929 (1987).
12. J. L. Thomas, D. L. Bonhaus, W. K. Anderson, C. L. Rumsey, and R. T. Biedron, *An O(Nm^2) Plane Solver for the Compressible Navier–Stokes Equations*, AIAA Paper 99-0785 (AIAA Press, Washington, DC, 1999).
13. J. R. Edwards and J. L. Thomas, *Development and Investigation of O(Nm^2) Preconditioned Multigrid Solvers for the Euler and Navier–Stokes Equations*, AIAA Paper 99-3263 (AIAA Press, Washington, DC, 1999).
14. S. R. Allmaras. *Multigrid for the 2-D Compressible Navier–Stokes Equations*, AIAA Paper 99-3336 (AIAA Press, Washington, DC, 1999).

15. S. G. Sheffer, L. Martinelli, and A. Jameson, An efficient multigrid algorithm for compressible reactive flows, *J. Comput. Phys.* **144**, 484 (1998).
16. J. R. Edwards, *Advanced Implicit Algorithms for Finite Rate Hydrogen–Air Combustion Calculations*, AIAA Paper 96-3129 (AIAA Press, Washington, DC, 1996).
17. C. J. Jachimowski, *An Analytical Study of the Hydrogen–Air Reaction Mechanism with Application to Scramjet Combustion*, NASA TP 2791, (NASA, 1988).
18. J. W. Wilson and R. W. MacCormack, Modeling supersonic combustion using a fully implicit numerical method, *AIAA J.* **30**, 1008 (1992).
19. R. W. Bilger, S. H. Starner, and R. J. Kee, On reduced mechanisms for methane–air combustion in nonpremixed flames, *Combust. Flame* **80**, 135 (1990).
20. I. M. Kennedy, C. Yam, D. C. Rapp, and R. J. Santoro, Modeling and measurement of soot formation in laminar diffusion flame, *Combust. Flame* **107**, 368 (1996).
21. T. J. Coakley and P. G. Huang, *Turbulence Modeling for High Speed Flows*, AIAA Paper 92-0436 (AIAA Press, Washington, DC, 1992).
22. J. S. Shuen, Upwind differencing and LU factorization for chemical non- equilibrium Navier–Stokes equations, *J. Comput. Phys.* **99**, 233 (1992).
23. S. S. Girimaji, *A Simple Recipe for Modeling Reaction-Rates in Flows with Turbulent Combustion*, AIAA Paper 91-1792 (AIAA Press, Washington, DC, 1991).
24. R. L. Gaffney, Jr., J. A. White, and S. S. Girimaji. *Modeling Turbulent Chemistry Interactions Using Assumed PDF Method*, AIAA Paper 92-3638 (AIAA Press, Washington, DC, 1992).
25. R. A. Baurle and S. S. Girimaji, *An Assumed PDF Turbulence-Chemistry Closure with Temperature–Composition Correlations*, AIAA Paper 99-0928 (AIAA Press, Washington, DC, 1999).
26. R. A. Baurle, *Modeling of Turbulent Reacting Flows with Probability Density Functions for Scramjet Applications*, Ph.D. thesis (North Carolina State University, Raleigh, NC, 1995).
27. Y. Ju, Lower-upper scheme for chemically treacting flow with finite-rate chemistry, *AIAA J.* **33**, 1418 (1995).
28. S.-T. Yu, Y.-L. Tsai, and J. S. Shuen, Three-dimensional calculations of supersonic reacting flows using an LU scheme, *J. Comput. Phys.* **101**, 276 (1992).
29. P. Gerlinger, J. Algermissen, and D. Brüggemann, Matrix dissipation for central difference schemes with combustion, *AIAA J.* **33**, 1865 (1996).
30. K. Sinha and G. V. Candler, *Convergence Improvement of Two-Equation Turbulence Model Calculations*, AIAA Paper 98-2649 (AIAA Press, Washington, DC, 1998).
31. R. Radespiel and R. C. Swanson, Progress with multigrid schemes for hypersonic flow problems, *J. Comput. Phys.* **116**, 103 (1995).
32. A. Jameson, W. Schmidt, and E. Turkel, *Numerical Solution of the Euler Equations by Finite Volume Methods Using Runge–Kutta Time Stepping Schemes.* AIAA paper 81-1259 (AIAA Press, Washington, DC, 1981).
33. R. C. Swanson and E. Turkel, On central difference and upwind schemes, *J. Comput. Phys.* **101**, 292 (1992).
34. P. Gerlinger and D. Brüggemann, An implicit multigrid scheme for the compressible Navier–Stokes equations with low-Reynolds-number turbulence closure, *J. Fluids Eng.* **120**, 257 (1998).
35. J. R. Narayan and S. S. Girimaji, *Turbulent Reacting Flow Computations Including Turbulence Chemistry Interactions*, AIAA-paper 92-0342 (AIAA Press, Washington, DC, 1992).
36. J. S. Evans, C. J. Schexnayder, and H. J. Beach, *Application of a Two-Dimensional Parabolic Computer Program to Prediction of Turbulent Reacting Flows*, NASA, TP 1169 (NASA, 1978).